

This is a repository copy of Mapping the role of monomer conformation in amyloid formation of  $\alpha$ -synuclein splice variants.

White Rose Research Online URL for this paper: <a href="https://eprints.whiterose.ac.uk/id/eprint/233284/">https://eprints.whiterose.ac.uk/id/eprint/233284/</a>

Version: Accepted Version

### **Article:**

Dewison, K., Taylor, A., Brockwell, D. et al. (1 more author) (Accepted: 2025) Mapping the role of monomer conformation in amyloid formation of  $\alpha$ -synuclein splice variants. Journal of the American Chemical Society. ISSN: 0002-7863 (In Press)

#### Reuse

Items deposited in White Rose Research Online are protected by copyright, with all rights reserved unless indicated otherwise. They may be downloaded and/or printed for private study, or other acts as permitted by national copyright laws. The publisher or other rights holders may allow further reproduction and re-use of the full text version. This is indicated by the licence information on the White Rose Research Online record for the item.

#### **Takedown**

If you consider content in White Rose Research Online to be in breach of UK law, please notify us by emailing eprints@whiterose.ac.uk including the URL of the record and the reason for the withdrawal request.



1	Mapping the Role of Monomer Conformation in Amyloid Formation of
2	α-synuclein Splice Variants
3	
4	Katherine M. Dewison, Alexander I. P. Taylor, David J. Brockwell*, Sheena E. Radford*
5	Astbury Centre for Structural Molecular Biology and School of Molecular and Cellular Biology,
6	Faculty of Biological Sciences, University of Leeds, Leeds, LS2 9JT, UK
7	
8	<b>Keywords</b> : Amyloid, α-synuclein, molecular dynamics, conformation, ionic strength, kinetics
9	
10	
11	
12	
13	
14	
15	
16	
17	

### Abstract

Amyloid formation of the protein  $\alpha$ -synuclein ( $\alpha$ Syn) is a hallmark of pathogenesis in Parkinson's disease, Multiple System Atrophy, and Dementia with Lewy bodies. Research has predominantly focused on the 140-amino acid  $\alpha$ Syn sequence, yet the SNCA gene can be alternatively spliced to generate several different isoforms, including  $\alpha$ Syn $\Delta$ 3,  $\alpha$ Syn $\Delta$ 5, and  $\alpha$ Syn $\Delta$ 3 $\Delta$ 5. Here we have used experimental and computational approaches to characterise these splice variants, in addition to the full-length  $\alpha$ Syn, in terms of their monomer conformation and amyloid propensity as a function of changes in ionic strength. Kinetic analysis of amyloid formation, flow-induced dispersion analysis, and coarse-grained molecular dynamics simulations reveal a striking correlation between monomer conformation and the rate of secondary nucleation of amyloid formation, and we show that this is governed by both global conformation of the polypeptide chain and local contacts in the hydrophobic core domain and acidic C-terminal domain. By combining changes in amino acid sequences and ionic strength, our analysis reveals the importance of local contacts and long-range electrostatic interactions in driving the kinetics of amyloid formation of  $\alpha$ Syn.

### Introduction

Parkinson's disease (PD), Multiple System Atrophy (MSA), and Dementia with Lewy bodies (DLB) are conditions categorised as 'synucleinopathies', which exhibit hallmark intracellular aggregates of  $\alpha$ -synuclein ( $\alpha$ Syn)<sup>1</sup>. Given the prominence of these amyloid aggregates in synucleinopathies, they are hypothesised to play a role in disease<sup>2–4</sup>, and are key markers of pathogenesis. Despite many efforts to develop therapeutics that target  $\alpha$ Syn aggregation, none have been successful to date<sup>5</sup>, highlighting that a better understanding of the molecular mechanisms underlying the aggregation of  $\alpha$ Syn into amyloid and the aetiology of synucleinopathies are needed. Attempts to develop this understanding have included studying the role of familial disease variants<sup>6,7</sup>, disease-relevant truncations<sup>8–10</sup>, membranes<sup>11–16</sup>, variants that have been designed based on *in silico* predictions of aggregation<sup>17–19</sup>, and the addition of chaperones<sup>20,21</sup>, nanobodies<sup>22,23</sup>, and other  $\alpha$ Syn-binding peptides<sup>24</sup> in the mechanism of amyloid formation.

The full-length 140-amino acid  $\alpha$ Syn protein is comprised of three domains: an amphipathic N-terminal domain (residues 1-60) that is required for membrane-binding<sup>25,26</sup> and facilitates the physiological function of  $\alpha$ Syn in membrane vesicle fusion at the synapse<sup>27–29</sup>; the hydrophobic core domain (residues 61-95, commonly referred to as the non-amyloid  $\beta$  component (NAC)<sup>30</sup>), which is necessary and sufficient to form amyloid<sup>31</sup>; and the highly acidic C-terminal domain (residues 96-140), which binds metal ions<sup>32,33</sup>, functions in SNARE complex assembly<sup>34</sup>, and is thought to protect  $\alpha$ Syn from amyloid formation<sup>8,9</sup>. The three biochemically distinct regions of  $\alpha$ Syn, which together facilitate functional 'promiscuity'<sup>35</sup>, results in a protein with a polarised sequence that is prone to self-assemble into amyloid fibrils.

The role of sequence length variation in the self-assembly and disease-context of a number of amyloidogenic proteins has been widely investigated hitherto, these include examples such as

the 3R and 4R splice variants of tau being implicated in different diseases<sup>36</sup>, the processing of amyloid-β to between 39 and 43 amino acids controlling its amyloidogenicity and involvement in disease<sup>37</sup>, and naturally-occurring C-terminal truncations of αSyn dramatically accelerating the rate of amyloid formation<sup>8,9,38</sup>. Although most research characterising the mechanisms of αSyn amyloid formation have focused on the 140-amino acid sequence, the gene encoding αSyn, SNCA, can be spliced to generate at least three alternative isoforms<sup>39,40</sup> (Figure 1). Specifically, exon 3 (encoding residues 41 to 54) and exon 5 (encoding residues 103 to 130) can be spliced in or out of the final transcript to generate either full-length αSyn (αSynFL, which contains residues encoded by both exons 3 and 5) or  $\alpha Syn\Delta 3$ ,  $\alpha Syn\Delta 5$  and  $\alpha Syn\Delta 3\Delta 5$ . The expression levels of the alternative splice variants across different brain regions and diseases (as revealed by mRNA levels) have been characterised in several publications<sup>41–46</sup> (Table S1). While some of these results indicate that the expression levels are changed in disease, others report similar levels between disease and control tissue samples. Furthermore, it should be noted that the presence of these variants in the pathological lesions of synucleinopathies (Lewy bodies or glial cytoplasmic inclusions) has not yet been reported, and their impact in disease aetiology remains to be determined. Despite this, recent work has demonstrated that these variants display distinct aggregation propensities 47-49 and MSA-associated single nucleotide polymorphisms in the non-coding regions of the SNCA gene lead to upregulation of  $\alpha Syn\Delta 5^{50}$ . Along with evidence that this variant is indeed translated in the brain<sup>51</sup>, this highlights the importance of better understanding of the amyloid formation mechanisms of these variants and their roles in the pathogenesis of synucleinopathies.

82

62

63

64

65

66

67

68

69

70

71

72

73

74

75

76

77

78

79

80

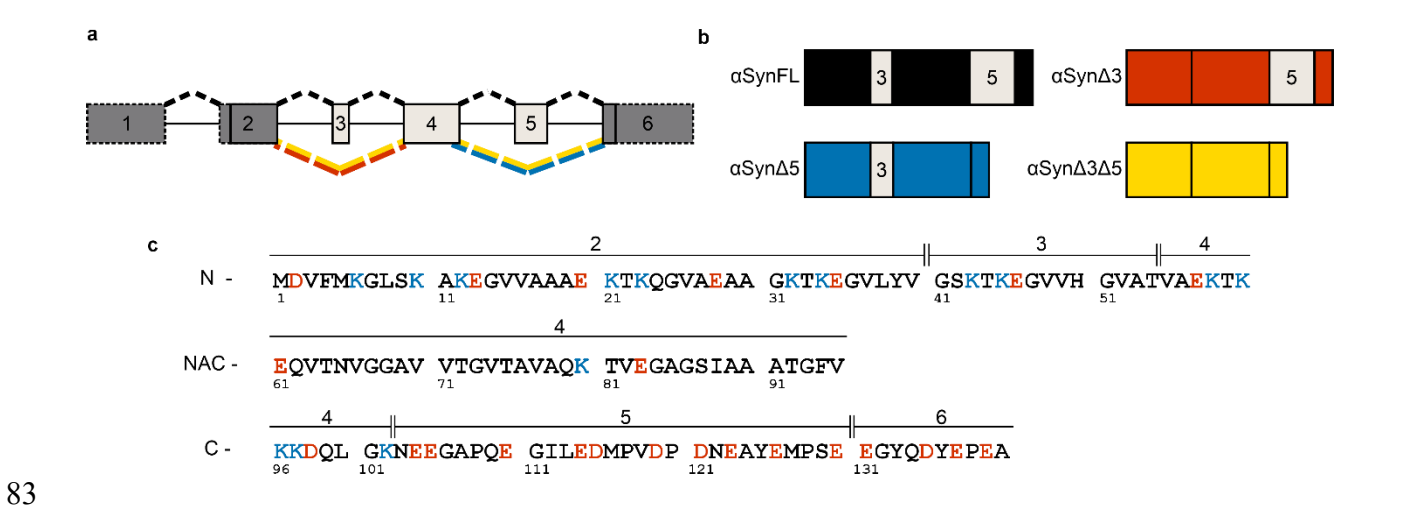


Figure 1. Alternative splice variants of  $\alpha$ Syn used in this work. (a) Schematic representation of SNCA. The boxes represent exons (1-6) and the solid lines represent introns. Dark grey boxes are constitutively spliced in, but light grey boxes are cassette exons. Boxes surrounded by dashed lines show exons that are not translated, boxes with solid lines show exons that are translated. αSynFL is generated by the splicing path indicated by the black dashed lines above the exons/introns. Alternative splicing is achieved by exon skipping (shown by coloured dashed lines) of either exon 3 (red), exon 5 (blue), or both exons 3 and 5 (yellow). Note that although an additional exon has been identified in the 5' untranslated region of SNCA (NCBI accession number NG 011851), previous publications have continued to refer to the exons as outlined in (a), so we have upheld this nomenclature for ease of comparison. (b) Representation of the proteins generated from alternative splicing of SNCA. Where cassette exons are included in the protein they are labelled with their exon number. (c) Amino acid sequence of αSyn, with the corresponding exons in which they are encoded displayed above and the domain indicated to the left (N = N-terminal domain, NAC = hydrophobic core domain, C = C-terminal domain). Negatively charged residues are coloured in red, and positively charged residues are coloured in blue.

85

86

87

88

89

90

91

92

93

94

95

96

97

Here, we set out to investigate how the monomer conformation of  $\alpha$ Syn splice variants influences their amyloidogenicity. Given the distinct sequence patterning of the three domains of  $\alpha$ Syn (Figure 1c), and the fact that  $\alpha$ SynFL is known to form transient long-range intramolecular electrostatic interactions in its monomeric state<sup>52–55</sup> that must be significantly perturbed by deletion of residues encoded by exons 3 and/or 5, we examined the effect of ionic strength on the rate and mechanisms of amyloid formation of the different variant sequences. Supported by global conformational measurements using flow-induced dispersion analysis (FIDA)<sup>56</sup> and coarsegrained molecular dynamics (MD) simulations using the CALVADOS 2 force field<sup>57,58</sup>, we reveal a striking correlation between monomer conformation and the rate of amyloid formation that is consistent across all splice variants and ionic strengths. Our analysis shows that changes in the global conformations of  $\alpha$ Syn are coupled to changes in local contacts; and furthermore, that interactions within the NAC and C-terminal regions critically alter the rate of secondary nucleation of amyloid formation. Together, these features rationalise the strikingly different amyloid propensities of the splice variants.

#### Results

# Residues encoded by exons 3 and 5 of SNCA have distinct effects on amyloid formation

To investigate the amyloid potential of the alternative splice variants of  $\alpha$ Syn, we generated recombinant proteins in which the amino acid sequences corresponding to exon 3 ( $^{41}$ GSKTKEGVVHGVAT<sup>54</sup>) and/or exon 5 ( $^{103}$ NEEGAPQEGILEDMPVDPDNEAYEMPSE<sup>130</sup>) are deleted (Figure 1). The rate of amyloid formation for each of these variants was then monitored using thioflavin T (ThT) fluorescence at starting monomer concentrations ranging from 20  $\mu$ M to 100  $\mu$ M (Figure 2a). In accord with previous findings<sup>47</sup>, the time to reach half the maximal

fluorescence (T<sub>50</sub>, Experimental Section, Table S2) of αSynFL and αSynΔ3 are similar and concentration-dependent over this range (Figure 2b), and we find that the calculated scaling exponents (the gradient of the log  $T_{50}$  vs log [ $\alpha$ Syn], see Experimental section, Eqn 1) are -0.55 and -0.49, respectively (Table S3). We then used the fitting platform AmyloFit to compare four different models of amyloid assembly for these two variants: elongation dominated, secondary nucleation dominated, fragmentation dominated, and multi-step secondary nucleation dominated assembly  $^{59}$  (Figure S1) . For  $\alpha SynFL$ , secondary nucleation, fragmentation, and multi-step secondary nucleation-dominated models achieved similarly good fits. For  $\alpha Syn\Delta 3$ , the model comparison favoured multi-step secondary nucleation. By contrast,  $\alpha Syn\Delta 5$  and  $\alpha Syn\Delta 3\Delta 5$  form amyloid more rapidly than  $\alpha SynFL$  and  $\alpha Syn\Delta 3$  and exhibited only minor changes in the rate of amyloid formation across the range of concentrations used (Figure 2a,b and Table S2), such that the scaling exponents for these variants is closer to zero ( $\gamma = 0.17$  and -0.064 for  $\alpha Syn\Delta 5$  and  $\alpha Syn\Delta 3\Delta 5$ , respectively (Table S3)) and for  $\alpha Syn\Delta 5$  this concentration-independence is also observed at lower monomer concentrations (from 2.5 µM to 20 µM (Figure S2)). The lack of concentration-dependence of the rate of amyloid formation by  $\alpha Syn\Delta 5$  and  $\alpha Syn\Delta 3\Delta 5$  suggests saturation of primary and/or secondary nucleation, such that conformational conversion from the fibril-bound monomer to the fibrillar state, rather than binding to catalytic sites, is the ratedetermining step. For all variants, insoluble fibrillar material was formed at the end of the reaction as judged by a pelleting assay and negative stain EM (Figure 2c,d, Table S5).

142

123

124

125

126

127

128

129

130

131

132

133

134

135

136

137

138

139

140

141

143

144

145

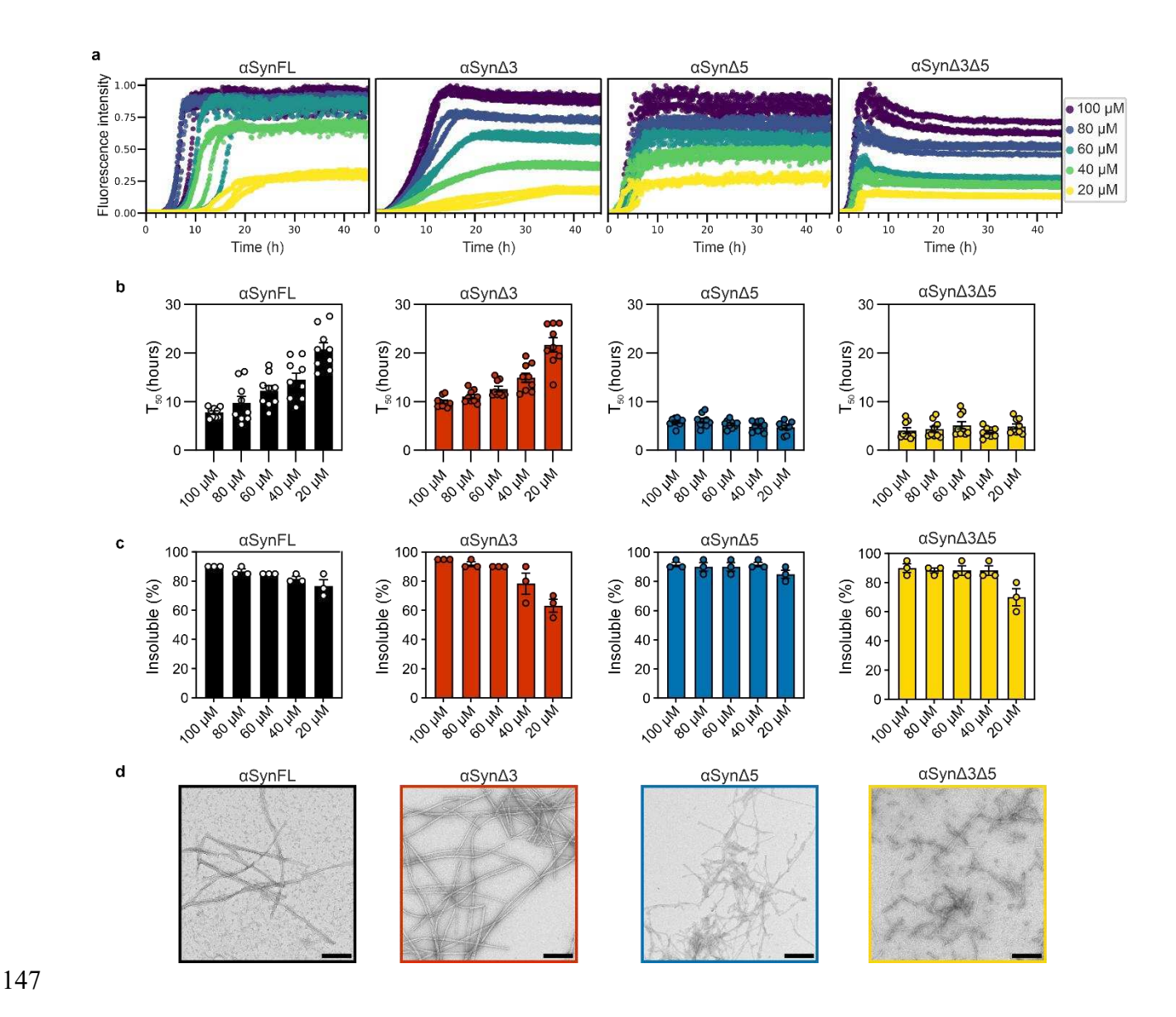


Figure 2. *De novo* fibril formation at different protein concentrations for the alternative splice variants of αSyn. (a) ThT fluorescence versus time for each of the variants (variant name indicated at the top of the plot) at monomer concentrations ranging from 20 μM to 100 μM (see key) in PBS (137 mM NaCl, 2.7 mM KCl, 8.1 mM Na<sub>2</sub>HPO<sub>4</sub>, and 1.5 mM KH<sub>2</sub>PO<sub>4</sub>; pH 7.4). Data are normalised to the maximum fluorescence intensity of each variant at 100 μM protein concentration. (b) Time to reach 50% of the maximum fluorescence (T<sub>50</sub>) for each condition. Individual values from three repeats, each containing three replicates, are plotted. The mean is

represented by the bar height and the error bars show standard error of the mean (SEM). (c) Percent insoluble material at the end point of ThT reactions as quantified using a pelleting assay (Experimental Section), where each data point corresponds to a ThT repeat and the error bar is SEM. (d) Negative stain transmission electron microscopy (TEM) images of the material formed at the end of the ThT assay for each variant. Scale bar, 250 nm.

We next investigated the capacity of the alternative splice variants to cross-seed the assembly of αSynFL monomer into amyloid. The justification for this is that the SNCA mRNA isoform encoding αSynFL constitutes ~95-97% of all SNCA mRNA transcripts that are expressed in the brain<sup>60</sup>, but whether the lowly-populated splice variants, particularly the more amyloidogenic  $\alpha Syn\Delta 5$  and  $\alpha Syn\Delta 3\Delta 5$ , are capable of triggering conversion of  $\alpha SynFL$  into amyloid under the conditions of these experiments was unknown. To test this, amyloid fibrils formed at the end of the de novo self-assembly reactions of each variant (at 100 µM protein concentration) were collected and sonicated to generate short fibril seeds (Experimental Section). The preformed fibril fragments were then added to  $\alpha SynFL$  monomers at a fibril seed concentration of 10% ( $\nu/\nu$ ) (monomer equivalent) and ThT fluorescence was used to monitor fibril formation (quiescent conditions, wherein elongation is the dominant mechanism of seeded growth<sup>61</sup>). As a control, selfseeding experiments (where the identity of the fibril seed was the same as the added monomer) were performed to show that the added fibrils could recruit their own monomer (Figure S3). Remarkably, and consistent with previous findings<sup>49</sup>, the only cross-seeding reaction that resulted in a significant increase in ThT fluorescence and the presence of fibrils at the end of the reaction was αSynFL monomer in the presence of αSynΔ5 fibril seeds (Figure 3, Table S6). Hence, the residues encoded by exon 3 (41GSKTKEGVVHGVAT<sup>54</sup>) are required for the αSyn variants to cross-seed fibril formation of the full-length protein monomers. These residues are form part of the fibril core in many of the resolved  $\alpha$ Syn amyloid structures<sup>62,63</sup>, potentially rationalising why  $\alpha$ SynFL is unable to adopt the same amyloid fold as  $\alpha$ Syn $\Delta$ 3 or  $\alpha$ Syn $\Delta$ 3 $\Delta$ 5 in the process of elongation.

161

162

163

164

165

166

167

168

169

170

171

172

173

174

175

176

177

178

179

180

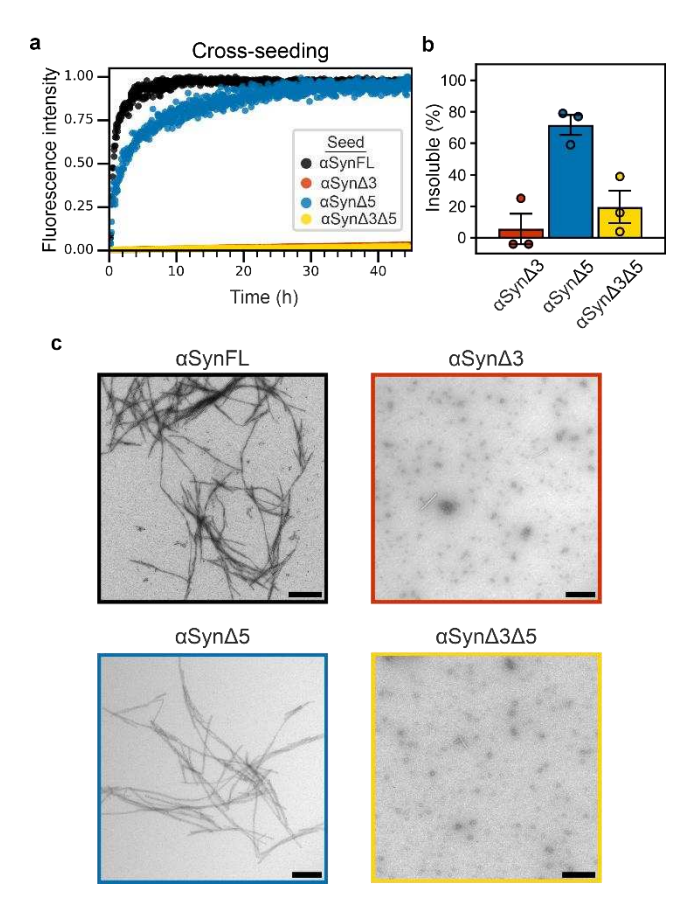
181

182

183

These results show that the residues encoded by exon 5 have a stronger impact on the rate of *de novo* amyloid formation than those encoded by exon 3, but those encoded by exon 3 modulate

recruitment of the  $\alpha$ SynFL monomer to fibrils. Hence, the different regions of the  $\alpha$ Syn sequence regulate different processes of amyloid formation, with the effect of removing one region being dependent on the context of the remaining sequence.



Representative ThT fluorescence traces of  $\alpha$ SynFL monomer and the fibril seed (type indicated in the key) in PBS. Data are normalised to the maximum intensity of the well if seeding occurred (based on ThT fluorescence, pelleting assay, and negative stain TEM) or to the maximum intensity measured from all conditions if seeding did not occur. (b) Quantification of the percent insoluble

material formed during the cross-seeding reaction and (c) representative negative stain TEM

**Figure 3.** Cross-seeding of the alternative splice variants of  $\alpha$ Syn with  $\alpha$ Syn monomer. (a)

images of the material formed. Scale bar, 250 nm.

## The ionic strength dependence of amyloid formation

Long-range interactions between the amphipathic N-terminal domain and highly-acidic C-terminal domain of monomeric  $\alpha$ Syn have been reported to regulate its amyloid formation<sup>52–55</sup>. The splice variants have stark differences in their charge-related sequence properties (Table S7), suggesting that alternative splicing could affect the monomer conformation and thus the amyloidogenicity of  $\alpha$ Syn. Specifically, there is a single His residue, one negatively charged and two positively charged residues in the 14-residue exon 3 (absent in  $\alpha$ Syn $\Delta$ 3 and  $\alpha$ Syn $\Delta$ 3 $\Delta$ 5), and ten negatively charged residues in the 28-residue exon 5 (absent in  $\alpha$ Syn $\Delta$ 5 and  $\alpha$ Syn $\Delta$ 3 $\Delta$ 5) (Figure 1c). To determine how the monomer conformation of the splice variants influences their amyloidogenicity, we next examined the effect of changing the ionic strength on the rate of the different pathways of amyloid formation for each splice variants.

The ionic strength dependence of amyloid formation of the different splice variants are shown in Figure 4a. All variants formed amyloid under all conditions, except for  $\alpha \mathrm{Syn}\Delta 3$  in 0 mM NaCl. Empirical fitting of the ThT fluorescence curves using a previously established general equation for accumulation of amyloid fibril mass (Figure S4, Experimental section Eqn 2)<sup>64</sup> was used to extract the macroscopic rate parameters  $\lambda$  and  $\kappa$  (Figure 4b, Figure S5, Figure S6, and Table S8), which describe the collective rate of the primary and secondary pathways of amyloid formation, respectively. The primary pathway is the sequence of primary nucleation and elongation by which *de novo* amyloid fibrils first form, whereas the secondary pathway is the positive feedback cycle of secondary processes (secondary nucleation and fragmentation) and elongation that results in exponential accumulation of fibril mass in the growth phase<sup>64</sup>. While the rate of the primary pathway ( $\lambda$ ) decreases approximately twenty-fold from 0 mM NaCl to 400 mM NaCl for  $\alpha \mathrm{SynFL}$ , there is little or no ionic strength dependence of  $\lambda$  for the other variants (Figure

S5, Table S8). By contrast, the rate of the secondary pathway ( $\kappa$ ) of all variants increases at lower ionic strength for all variants and saturates at NaCl concentrations greater than 200 mM for all variants except for  $\alpha \text{Syn}\Delta 3$  (Figure 4b). Our analyses of the fitting error (Figure S6) show us that we can be confident in the best-fit  $\lambda$  and  $\kappa$  values (Figure 4b and Figure S5). Despite this, there is a high degree of inter-replicate variability in  $\lambda$ , likely arising from confounding well-to-well experimental variation (e.g. the surface of the beads used to promote primary nucleation).

218

219

220

221

222

223

224

225

226

227

228

229

230

231

232

233

234

235

236

237

238

239

The values of  $\kappa$  are notably different between the variants. While deletion of exon 3 can either increase or decrease κ depending on sequence context, deletion of exon 5 consistently causes an increase in  $\kappa$ , with an ~1.2-fold increase in  $\kappa$  across all ionic strengths for  $\alpha Syn\Delta 5$  compared with  $\alpha \text{SynFL}$ , and an >2.5-fold increase in  $\kappa$  for  $\alpha \text{Syn}\Delta 3\Delta 5$  compared with  $\alpha \text{Syn}\Delta 3$ . The difference between  $\alpha Syn\Delta 3\Delta 5$  and  $\alpha Syn\Delta 3$  is more extreme at lower ionic strengths, with  $\kappa$  ten-fold higher for  $\alpha \text{Syn}\Delta 3\Delta 5$  in 50 mM NaCl. As expected from these data, the percent of insoluble material formed at the end of the ThT assay for  $\alpha Syn\Delta 3$  is also dependent on ionic strength, with no fibrils forming in 0 mM NaCl, while fibrils resulted in 50 mM NaCl (Figure 4c,d, and Table S9). Negative stain TEM also showed that whilst aSynFL forms long amyloid fibrils in 0 mM NaCl, the fibrils are visibly shorter in 400 mM NaCl (although length could not be quantified due to fibril clumping), supporting the kinetic data that the rate of secondary processes increases with ionic strength (Figure 4d). The discrepancy between the rate of fragmentation and the measured rate of secondary processes in de novo assembly can be calculated from the ratio between the observed and expected absolute change in the rate of elongation, k, i.e. (0.072-0.036)/(7.10-0.036) for  $\alpha$ SynFL and (0.061-0.036)/(0.325-0.036) for  $\alpha$ Syn $\Delta$ 3. This shows that the rate of fragmentation is approximately 200-times ( $\alpha SynFL$ ) and 10-times ( $\alpha Syn\Delta 3$ ) too low to explain the  $\kappa$  values

observed in *de novo* assembly, showing that secondary nucleation is the dominant process for  $\alpha SynFL$  and  $\alpha Syn\Delta 3$  under our conditions.

 $\alpha Syn\Delta 5$  and  $\alpha Syn\Delta 3\Delta 5$  flocculate during amyloid formation – shown by the decrease in ThT fluorescence signal in the plateau phase (Figure 4a) and negative stain TEM images (Figure 4d), consistent with previous observations with other C-terminal truncation variants<sup>9</sup>. As a consequence, we were unable to perform the same analysis for these variants, leaving open the possibility that fragmentation could play a more important role for these sequences. However, as  $\kappa$  follows the same trend with ionic strength between the splice variants, it is most likely that the same mechanism controls their behaviour. Hence, we propose that secondary nucleation, not fragmentation, is the specific secondary process that is governed by ionic strength.

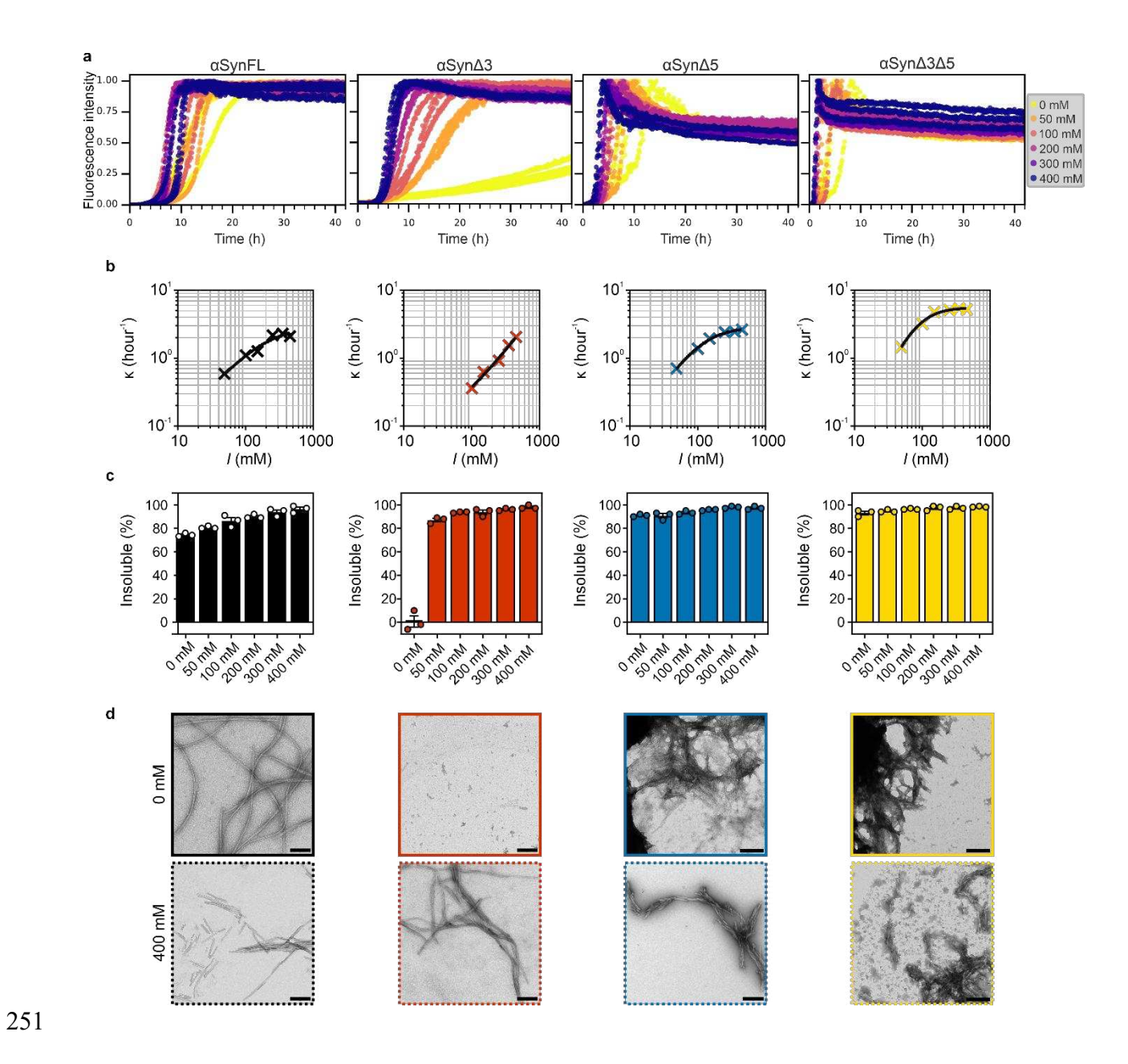


**Figure 4.** Ionic strength dependence of amyloid formation of αSyn and its splice variants. (a) Representative ThT fluorescence curves for the four splice variants (as indicated above each plot) in 20 mM sodium phosphate (pH 7.4) at NaCl concentrations ranging from 0 mM to 400 mM (shown in key). The starting αSyn monomer concentration was 100 μM. Data are normalised to the maximum intensity of the well, excluding αSyn $\Delta$ 3 at 0 mM NaCl, as a plateau was not reached within the 42 hours of the experiment – in this case, data are normalised to the maximum intensity

detected for the entire  $\alpha \text{Syn}\Delta 3$  dataset. (b)  $\kappa$  values derived from empirical fitting of the ThT curves using equation [2] (Experimental Section). Note that the error bars could not be plotted as they are smaller than the size of the symbol. The data are fitted using equation [8] (Experimental Section) and shown as the solid lines on the plots. The plotted ionic strength (*I*) is that of the total buffer. (c) Quantification of insoluble material at the end of the incubation period for each splice variant at each ionic strength. Each data point is the result of one biological repeat and the error bars are SEM. Note that in some case the SEM is too small to be seen on the plots. (d) Representative negative stain TEM images of the material formed during the ThT assays in 0 mM or 400 mM NaCl. Scale bar, 250 nm.

To better understand the underlying mechanism of the influence of ionic strength on secondary nucleation in fibril formation, the ionic strength dependence of  $\kappa$  was fitted to two plausible mathematical models applying Debye-Hückel theory to different steps of the fibril selfreplication process (Experimental Section and Supporting Information). In the 'Brønsted-Bjerrum' model, ions are assumed to stabilise monomer-fibril interactions, whereas in the 'Free Energy Barrier' model ions are assumed to stabilise a conformational transition state involved in templated conversion to the amyloid state. We note that these models do not mathematically distinguish between interactions/conversion on the fibril surface (i.e. secondary nucleation) or fibril ends (i.e. elongation), but as  $\lambda$  does not increase with ionic strength, we can conclude that the dominant change in interaction/conversion when interpreting these data is due to changes in the processes occurring at the fibril surface. Both models predict a positive relationship between κ and ionic strength, but only the 'Free Energy Barrier' model was able to reproduce the observed saturation of κ at higher ionic strengths (Figure 4b, Figure S8 and Table S10). This suggests that unfavourable electrostatic interactions, perhaps the alignment of like charges during fibril nucleation, contribute to the free energy barrier for templated conversion to the amyloid state  $(\Delta G^{\ddagger} = \Delta G^{\ddagger}_{charged} + \Delta G^{\ddagger}_{non-})$ charged), and screening of these unfavourable electrostatic interactions is responsible for the increase in  $\kappa$  with increasing ionic strength. The existence of a limit on  $\kappa$  at high ionic strength, on the other hand, intuitively suggests that there are also non-electrostatic factors that limit the rate of secondary nucleation. Using this model, we were also able to investigate the differences between the variants,

268

269

270

271

272

273

274

275

276

277

278

279

280

281

282

283

284

285

286

287

288

289

290

Using this model, we were also able to investigate the differences between the variants, separating out the electrostatic ( $\Delta G^{\ddagger}_{charged}$ ) and non-electrostatic ( $\Delta G^{\ddagger}_{non-charged}$ ) contributions to the free energy barrier (Table S11). Most notably, the saturated (i.e. fully screened) value of  $\kappa$  is increased for  $\alpha Syn\Delta 3\Delta 5$  relative to  $\alpha SynFL$  and  $\alpha Syn\Delta 5$  (Figure 4b). This suggests that the free

energy barrier that remains when any unfavourable electrostatic interactions are screened out is lower for  $\alpha Syn\Delta 3\Delta 5$  than for  $\alpha SynFL$  or  $\alpha Syn\Delta 5$ , implying that exon 3 makes additional unfavourable contributions to the free energy barrier that are independent of the electrostatics. In agreement with this, fitting with the favoured 'Free Energy Barrier' model suggested that  $\alpha Syn\Delta 3\Delta 5$  has a smaller  $\Delta G^{\ddagger}_{non-charged}$  than  $\alpha Syn\Delta 5$  ( $\Delta \Delta G^{\ddagger}_{non-charged} = -1.38 \pm 0.16$  RT). The lack of observed saturation up to  $\kappa = 2$  hr<sup>-1</sup> for  $\alpha Syn\Delta 3$  suggests that the same is true for this variant, and the model analysis also suggested that  $\alpha Syn\Delta 3$  has a smaller  $\Delta G^{\ddagger}_{non-charged}$  than  $\alpha SynFL$ , although the margin of error is much larger due to uncertainty regarding the exact limit that  $\kappa$  tends to at saturation ( $\Delta \Delta G^{\ddagger}_{non-charged} = -4.52 \pm 3.55$  RT). Taken together, the results suggest that the residues encoded by exon 3 (41GSKTKEGVVHGVAT<sup>54</sup>) make an additional unfavourable non-electrostatic contribution to the free energy barrier for conversion from fibril-bound monomer to the amyloid state, although the molecular origins of this effect remain unresolved.

It is also striking that fibrils did not form for  $\alpha Syn\Delta 3$  in 0 mM NaCl, whereas a quantitative (>87 ± 2%) conversion of monomer to insoluble material resulted at concentrations  $\geq$ 50 mM NaCl (Figure 4c,d), and the  $\kappa$  values were globally smaller for this protein compared with the other variants at all ionic strengths (Figure 4b). The simplest explanation for this observation is that  $\alpha Syn\Delta 3$  experiences additional inhibitory electrostatic interactions that either do not occur, or are adequately compensated for, in the other variants and are tunable by modifying the ionic strength. As  $\alpha Syn\Delta 3\Delta 5$  also lacks the residues encoded by exon 3, yet does not display this behaviour, it suggests that the reduction in  $\kappa$  for  $\alpha Syn\Delta 3$  results from the presence of a complete C-terminal region (containing exon 5) in addition to truncation of the N-terminal region (by deletion of residues encoded by exon 3), which would maximise charge imbalance. This demonstrates that the

consequence of exon splicing on the behaviour of  $\alpha Syn$  is dependent on the context of the remaining residues.

315

316

317

318

319

320

321

322

323

324

325

326

327

328

329

330

331

332

333

314

313

# The ionic strength dependence of monomer conformational properties

We next explored the influence of ionic strength on the conformational properties of the monomers of the alternative splice variants of αSyn. Using flow-induced dispersion analysis (FIDA) we measured the average hydrodynamic radii (R<sub>h</sub>) of the αSyn splice variants at different ionic strengths (Figure 5a, Figure S9). At the highest ionic strength (400 mM NaCl), at which concentration most electrostatic interactions are expected to be screened, all four variants had R<sub>h</sub> values that were ~0.3-0.4 nm smaller than predictions for fully unfolded proteins of the same lengths (Table S12)<sup>66</sup>, consistent with well-documented non-local interactions involving hydrophobic residues and/or transient secondary structure<sup>67,68</sup>. However, at low ionic strength (0 mM NaCl), a further pronounced compaction was observed for αSynFL (consistent with previous investigations using paramagnetic relaxation enhancement NMR<sup>17,52,55</sup>) and for  $\alpha$ Syn $\Delta$ 3, but not for  $\alpha Syn\Delta 5$  and  $\alpha Syn\Delta 3\Delta 5$  (Figure 5a, Table S12). For example,  $\alpha SynFL$  compacted from an  $R_h$ of 3.28  $\pm$  0.03 nm (400 mM NaCl) to 3.05  $\pm$  0.02 nm (0 mM NaCl), whereas  $\alpha Syn\Delta 5$  had corresponding  $R_h$  values of 2.91  $\pm$  0.02 nm (400 mM NaCl) and 2.88  $\pm$  0.01 nm (0 mM NaCl). This suggests that the residues encoded by exon 5 form non-local electrostatic interactions that drive global compaction of these variants at low ionic strength. This can be rationalised by the fact that ten negatively charged residues are encoded by exon 5. By contrast, inclusion or exclusion of the residues of exon 3 has little effect on the relationship between ionic strength and R<sub>h</sub>.

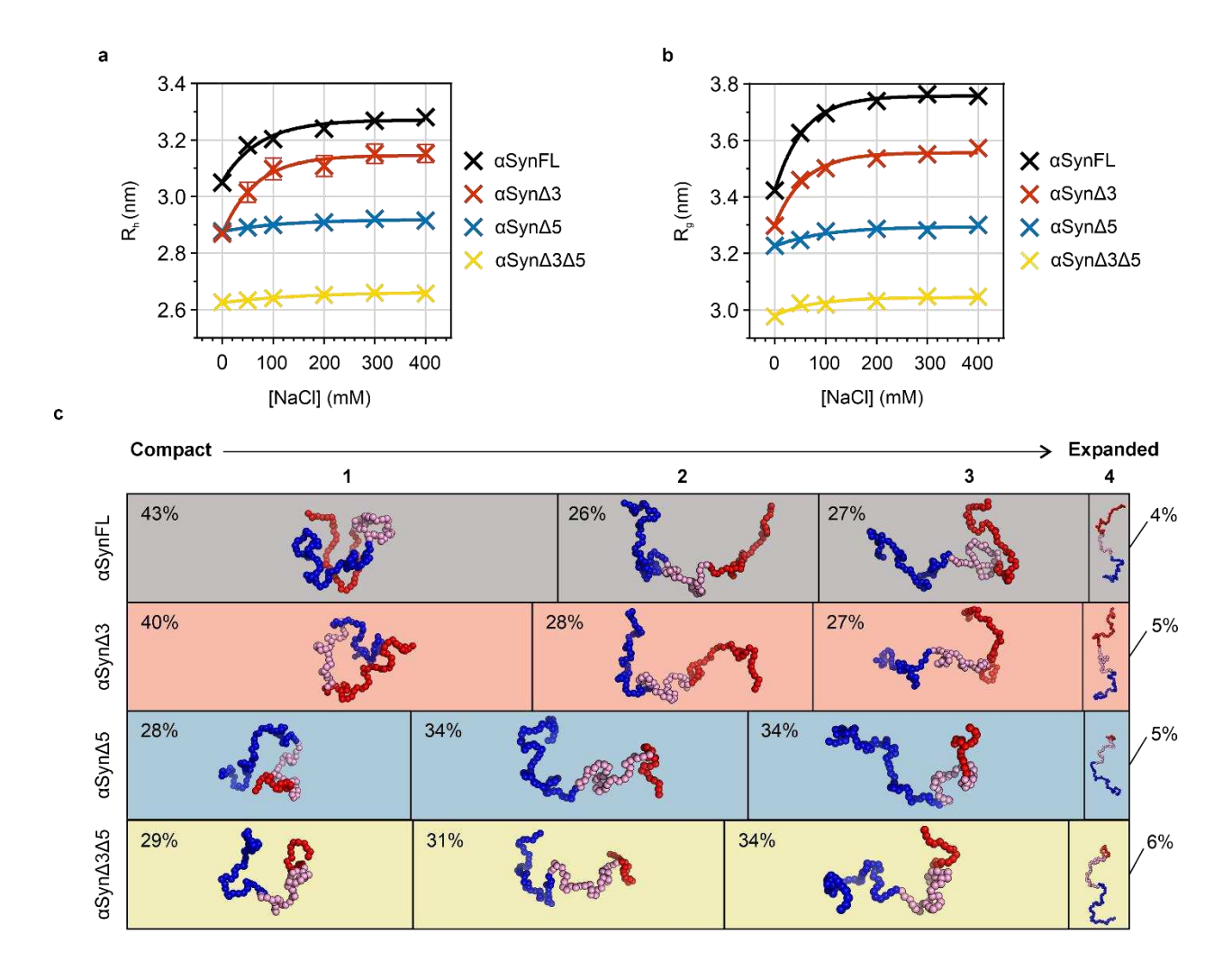


Figure 5. Monomeric conformers of the alternative splice variants of  $\alpha Syn$ . (a)  $R_h$  values of the alternative splice variants of  $\alpha Syn$  at different NaCl concentrations. Average  $R_h$  values for each condition were determined experimentally by FIDA (Experimental Section). Mean of  $R_h$  values from at least eight Taylorgrams and the SEM are plotted. A one phase exponential decay was fitted to the data in GraphPad Prism 10.1.2. (b) Average  $R_g$  of alternative splice variants of  $\alpha Syn$  at different ionic strengths in CALVADOS 2 simulations. Note that the ionic strength used for simulations is converted into equivalent NaCl concentration here, to aid comparison with a. (c) Classification of the conformational ensemble of the alternative splice variants of  $\alpha Syn$  using

spectral clustering, alongside representative conformers. The structural class 1 is the most compact cluster, with many interactions between the N-terminal, NAC and C-terminal domains. Class 2 is characterised by a reduction in interactions between the C-terminal domain and the N-terminal/NAC region. Class 3 has fewer interactions between the N-terminal domain and NAC/C-terminal region. Class 4 contains the most expanded conformations, which have the fewest interactions between all three domains. Percentage of the frames of each simulation of the alternative splice variants in each of the four structural classes is shown. The width of the boxes represents the proportion of frames that were categorised as being in the corresponding class, with percentages of frames indicated in the boxes. Data used here were from simulations at 49 mM ionic strength (equivalent to 20 mM sodium phosphate, 0 mM NaCl). The most representative frame (Experimental Section), in terms of global inter-residue distances, for each cluster for each variant is displayed within each box, with the N-terminal domain coloured blue, hydrophobic core domain (NAC) coloured pink, and the C-terminal domain in red.

To characterise the conformational ensembles of the variants at different ionic strengths, and to better understand the link between sequence, monomer conformation, and the rate and mechanism of amyloid formation, we carried out coarse-grained molecular dynamics (MD) simulations using the CALVADOS 2 force field  $^{57,58}$ . The CALVADOS 2 simulations predicted a change in compaction with sequence and ionic strength that shows a striking resemblance to the experimental FIDA data (Figure 5b, Table S13). In the simulation results, we characterised compaction using the radius of gyration (Rg) rather than Rh, as the former can be exactly calculated from analysis of simulation trajectories, whereas post-simulation analysis of Rh remains challenging (however, Rg and Rh are generally expected to scale closely with one another  $^{70,71}$ ). Analysis of the Flory exponents (v), which provide a length-independent measure of chain compaction  $^{72}$ , also confirmed a compact state (v < 0.5) for aSynFL and aSynΔ3 at low ionic strength, but an intermediate degree of compaction (v = 0.54) for aSynΔ5 and aSynΔ3Δ5 (Table S14).

We next analysed the simulation trajectories to obtain intramolecular  $C\alpha$ - $C\alpha$  contact probability maps, showing the proportion of time that each pair of residues spends within a threshold distance (20 Å) of each other. In agreement with previous experimental studies <sup>17,52,55,73</sup>, the contact maps of  $\alpha$ SynFL and  $\alpha$ Syn $\Delta$ 3 had strong contact probabilities between the N-terminal and C-terminal domains at low ionic strength (Figure S10). These interactions were abolished at higher ionic strengths (Figure S11) and were attenuated at all ionic strengths for the  $\alpha$ Syn $\Delta$ 5 and  $\alpha$ Syn $\Delta$ 3 $\Delta$ 5 variants, which lack exon 5 and thus 28 of the 45 residues of the C-terminal domain (Figure S10). In addition,  $\alpha$ Syn $\Delta$ 3 had a mild attenuation of interactions between the C-terminal domain and residues ~20 to 40 that juxtapose the missing exon 3, although the overall effect on the N- to C-terminal domain interaction propensity was much smaller than that caused by deletion

of exon 5 (Figure S10). Thus, the simulations show that favourable electrostatic interactions between the amphipathic N-terminal domain and acidic C-terminal domain, which contains exon 5, drive compaction of  $\alpha$ SynFL and  $\alpha$ Syn $\Delta$ 3 at low ionic strength.

381

382

383

384

385

386

387

388

389

390

391

392

393

394

395

396

397

398

399

400

401

402

403

To explore in more detail how the conformational ensembles differ between splice variants, we used spectral clustering to classify conformers within the simulation trajectories based on the similarity of their  $C\alpha$ - $C\alpha$  distances (Experimental Section). This allowed us to identify distinct compact, partially compact, and expanded species within the conformational ensembles of the  $\alpha$ Syn variants (Figure S12 and S13). It is important to note that  $\alpha$ Syn has a relatively smooth conformational energy landscape in our simulations, so that these states represent subdivisions of a spectrum of conformations in the energy landscape, rather than well-separated energy basins. Across all variants, we reproducibly identified four structural classes: a compact class involving N-C interactions; two partially compact classes with expanded N- or C-terminal domains; and an expanded class (Figure 5c). By quantifying the distribution of conformers (i.e. simulation frames) across each of these structural classes, we identified that at 49 mM ionic strength (equivalent to 20 mM sodium phosphate buffer, pH 7.4, 0 mM NaCl) αSynFL and αSynΔ3 were in their most compact class in 43% and 40% of the frames, respectively, while  $\alpha Syn\Delta 5$  and  $\alpha Syn\Delta 3\Delta 5$  were only in their most compact class for 28% and 29% of the frames, respectively (Figure 5c, Figure S13). This suggests that the presence of exon 3 at low ionic strength skews the conformational distribution of αSyn towards an enhanced population of structurally inter-related compact species involving long-range N-C interactions.

Overall, the results of the coarse-grained MD simulations suggest that a more expanded conformational ensemble with fewer long-ranged N-C interactions correlates with a higher rate of secondary nucleation and more rapid amyloid formation.

## Monomer conformation correlates with secondary nucleation of αSyn amyloid formation

404

405

406

407

408

409

410

411

412

413

414

415

416

417

418

419

420

421

422

423

424

425

426

We next explored whether, and how, the conformational properties of the different  $\alpha$ Syn monomers correlate with changes in their amyloid-forming ability at different ionic strengths. We examined the correlation between the experimental self-assembly data and three measures of the compaction and shape of the different  $\alpha$ Syn variants in the CALVADOS 2 simulations: the Flory exponent ( $\nu$ ), asphericity ( $\Delta$ ), and prolateness (S) (Table S14). We focused on these metrics as they are independent of chain length. Examples of conformations with different  $\Delta$  and S are shown in Figure S14.

We calculated these metrics for the different alternative splice variants across all ionic strengths tested and performed a Spearman's rank analysis with the parameters extracted from the amyloid formation assays: rate of the primary pathway  $(\lambda)$ , rate of the secondary pathway  $(\kappa)$ , and the percentage of insoluble material at the end of the experiment (Figure 6, Figure S15). The results were striking, revealing a clear, strong correlation between monomer conformation and amyloid formation. Although this correlation was evident between all three of the conformational properties  $(\Delta, S, \text{ and } v)$  and both  $\kappa$  and percentage of insoluble material, the strongest correlations were identified between the prolateness of the monomer (S) and secondary pathway of amyloid formation (κ), and also between the percentage of insoluble material and v, which each have a correlation coefficient of 0.85. Interestingly, the primary pathway of amyloid formation ( $\lambda$ ) correlated more weakly with  $\Delta$ , S, and v (correlation coefficients of 0.60, 0.68 and 0.32, respectively). Furthermore, for the latter correlations with  $\lambda$ , we note that when we consider individual variants, rather than the combined data, the correlations appear to disappear or even reverse (Figure S15), an example of Simpson's paradox<sup>74</sup>. Importantly, the positive correlations between k and the conformational properties of the monomer are consistent both within and upon

combining data for the different variants, so we can be more confident in interpretating these findings. Overall, this analysis suggests that the global link between monomer conformational properties and amyloidogenicity is specific for the secondary pathway of amyloid formation (specifically relating to the effect on secondary nucleation), and any relationship between ionic strength and the rate of the primary pathway is not shared between the four variants tested here.

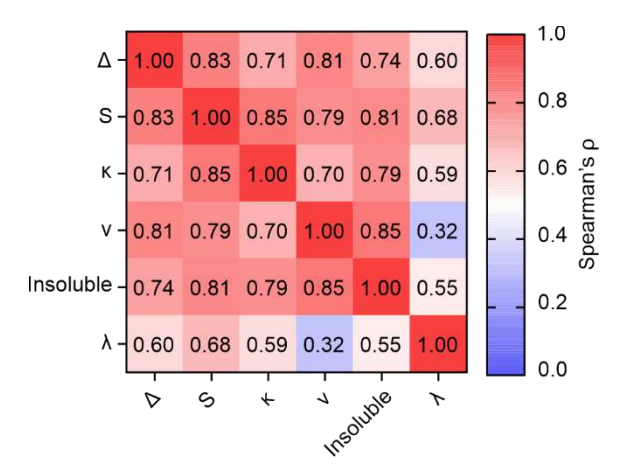


**Figure 6.** Spearman's  $\rho$  correlation coefficient heatmap of the parameters extracted from the ThT assay ( $\lambda$ ,  $\kappa$ , and insoluble material) and those predicted based on the CALVADOS 2 simulations ( $\Delta$ , S, and  $\nu$ ).

The calculated  $\kappa$  and predicted S values for  $\alpha \mathrm{Syn}\Delta 5$  and  $\alpha \mathrm{Syn}\Delta 3\Delta 5$  are larger than those for  $\alpha \mathrm{SynFL}$  and  $\alpha \mathrm{Syn}\Delta 3$  at all ionic strengths tested, which supports the notion that the C-terminal domain of  $\alpha \mathrm{Syn}$  protects against amyloid formation, perhaps by driving compaction and shielding the hydrophobic NAC domain<sup>8</sup>. It should be noted, however, that the results from this analysis do not explain the differences between  $\alpha \mathrm{SynFL}$  and  $\alpha \mathrm{Syn}\Delta 3$ , as the fitted  $\kappa$  values indicate that secondary nucleation is consistently faster for  $\alpha \mathrm{SynFL}$  compared with  $\alpha \mathrm{Syn}\Delta 3$  at all ionic strengths tested, yet  $\alpha \mathrm{Syn}\Delta 3$  is predicted by CALVADOS 2 to be relatively more expanded than  $\alpha \mathrm{SynFL}$  across the same range of ionic strengths. This suggests that the residues encoded by exon 3 (41-54) may play a role in regulating the rate of amyloid formation that is distinct from changes to the overall expansion of the protein, perhaps due to differences in the regions that form interactions more frequently (Figure S10).

Finally, we performed a Spearman's rank analysis to explore how inter-residue distances between all residue pairs correlate with the rate of the secondary processes,  $\kappa$ , for each variant across all ionic strengths (Figure S16). To determine if these relationships are conserved between the splice variants, we performed this analysis on data relating to inter-residue pairs common to all four variants (residues 1-40, 55-102, and 131-140 – yielding 1953 unique residue pairs) at all six ionic strengths. This revealed distinct correlation patterns for different regions of  $\alpha$ Syn (Figure 7a). Of note, increased inter-residue distances within the hydrophobic NAC domain correlate positively with  $\kappa$ , supporting the notion that increasing solvent-exposure of NAC is associated with an increased rate of amyloid formation via secondary nucleation. The residue pair whose  $C\alpha$ - $C\alpha$  distance correlates most positively with  $\kappa$  is Q79-E83 (Figure 7b), although nearby residue pairs are also strongly correlated with  $\kappa$ . By contrast, the inter-residue distances within the C-terminal domain correlate negatively with  $\kappa$  (i.e. closer distances are associated with an increase

in  $\kappa$ ). A more complex picture is seen in the N-terminal domain, with a mixture of local compaction and expansion correlating with  $\kappa$  (Figure 7a), likely due to differences between the individual variants in this region (Figure S16). The residue pair distance that correlates most negatively with  $\kappa$  is Y133-A140 (Figure 7c), although the effect was broadly distributed across all C-terminal residues that were included in the analysis, and thus likely encompasses the acidic C-terminal domain as a whole. Together, this analysis demonstrates that local expansion of NAC (particularly between Q79-E83) and compaction of the C-terminal domain correlate with a high rate of the secondary pathway of amyloid formation, and *vice versa*, enabling us to visualise the conformations of monomers associated with either a low (Figure 7d) or high (Figure 7e) value of  $\kappa$  and hence more rapid fibril formation via secondary nucleation.

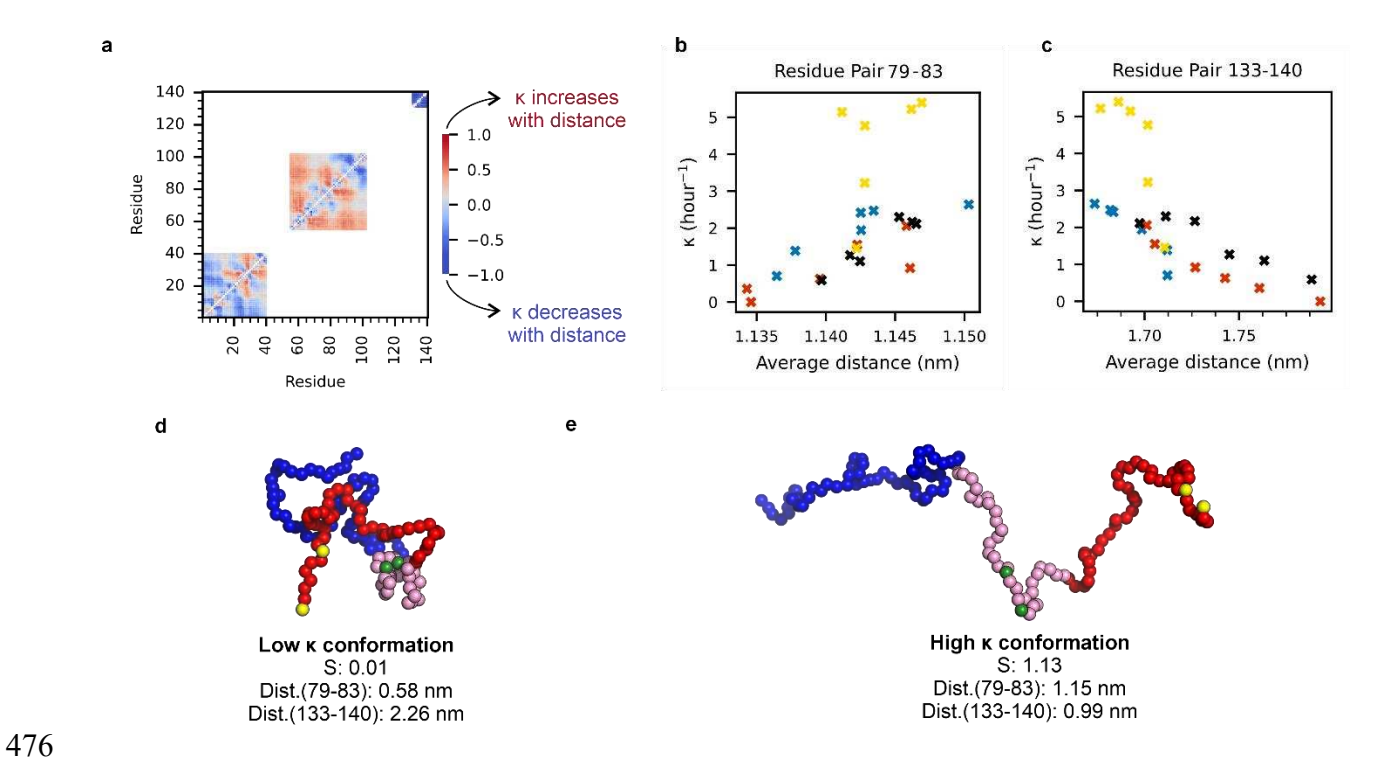


Figure 7. Inter-residue distances correlate with secondary nucleation in amyloid formation. (a) Spearman's rank heatmap of the inter-residue distances between all residue pairs of the alternative splice variants of αSyn from CALVADOS 2 simulations with experimentally derived  $\kappa$  values. Residues encoded by exons 3 or 5 and residue pairs that cross potentially spliced out regions are masked to prevent confounding results. (b)  $\kappa$  versus the average distances derived from the CALVADOS 2 simulations for the residue pair Q79-E83, whose inter-residue distance correlates the most positively with  $\kappa$ . (c) As in (b) for the residue pair Y133-A140, the residue pair that correlates the most negatively with  $\kappa$ . (d) Representative low  $\kappa$  state conformation of αSynFL, with a low S, short distance between residues 79-83, and long distance between residues 133-140. (e) Representative high  $\kappa$  state conformation of αSynFL, with a high S, long distance between residues 79-83, and short distance between residues 133-140. In (d) and (e), the N-terminal domain is shown in blue, the hydrophobic core domain shown in pink, and the C-terminal domain is shown in red. Residues 79 and 83 are shown in green and residues 133 and 140 are shown in yellow.

491

492

493

494

495

496

497

498

499

500

501

502

503

504

505

506

507

508

509

510

511

512

513

### Discussion

# Alternative sequences, conformational ensembles, and rates of amyloid formation

Here, using CALVADOS 2 simulations<sup>57,58</sup>, we provide a robust link between the global

conformation of monomeric  $\alpha$ Syn (as judged by the parameters:  $\nu$ ,  $\Delta$ , and S) and the rate of the secondary nucleation of amyloid formation that is displayed by all alternative splice variants analysed here (Figure 8). The compaction of αSyn monomers at low ionic strength (Figure 8a) has been shown previously using paramagnetic relaxation enhancement NMR experiments 17,52,55, and has been suggested to shield the NAC region and inhibit secondary nucleation<sup>75</sup>. In fact, αSyn(K6A;K10A;K12A), which attenuates electrostatic interactions between the N- and Cterminal domains, has been reported to be more expanded than αSynWT and forms amyloid at a faster rate<sup>75</sup>. Furthermore, we note that the notion of monomer conformation being an important determinant of amyloid formation has been described previously for other amyloidogenic proteins, including tau whose conformational expansion is also associated with the acceleration of amyloid formation<sup>76</sup>, while compaction of the polypeptide chain resulting from Zn<sup>2+</sup> binding (measured using ion mobility mass spectrometry) leads to an enhanced rate of amyloid formation for  $\alpha \text{Syn}^{77}$ . Our analyses support the model<sup>52</sup> that global compaction is driven largely by interactions between the N- and C-terminal regions of αSyn, and demonstrate that a more expanded monomer (and one with higher prolateness) correlates with increased  $\kappa$  (Figure 8b). The strong correlation of prolateness with secondary nucleation is interesting, as prolate conformers are 'stretched out' and thus have an exposed NAC region (Figure 7e, Figure S14b). On the thermodynamic side, it is also interesting that the Flory exponent (v) correlates most strongly with the percent insoluble material (Figure 6, Figure S15), as polymer theory predicts that v depends on affinity of the polypeptide chain for itself rather than the solvent, and is thus closely related to solubility<sup>72</sup>. That the increased prolateness associated with an increase in ionic strength does not also cause an acceleration of primary nucleation, as indicated by  $\lambda$ , is notable. For  $\alpha Syn\Delta 3$ ,  $\alpha Syn\Delta 5$ , and  $\alpha Syn\Delta 3\Delta 5$ , we observe minimal changes in  $\lambda$  over the range of ionic strengths tested here, suggesting that an exposed NAC region is not needed to form the initial interactions involved in primary nucleation, and that electrostatics do not strongly affect the energy barriers for primary nucleation and elongation, at least under our conditions. The one exception to this is  $\alpha SynFL$ , where there appears to be a weak inverse correlation between ionic strength and the rate of primary nucleation. This could reflect screening out of favourable inter-chain electrostatic interactions between the N- and C-termini of different monomers, which enable primary nucleation to occur.



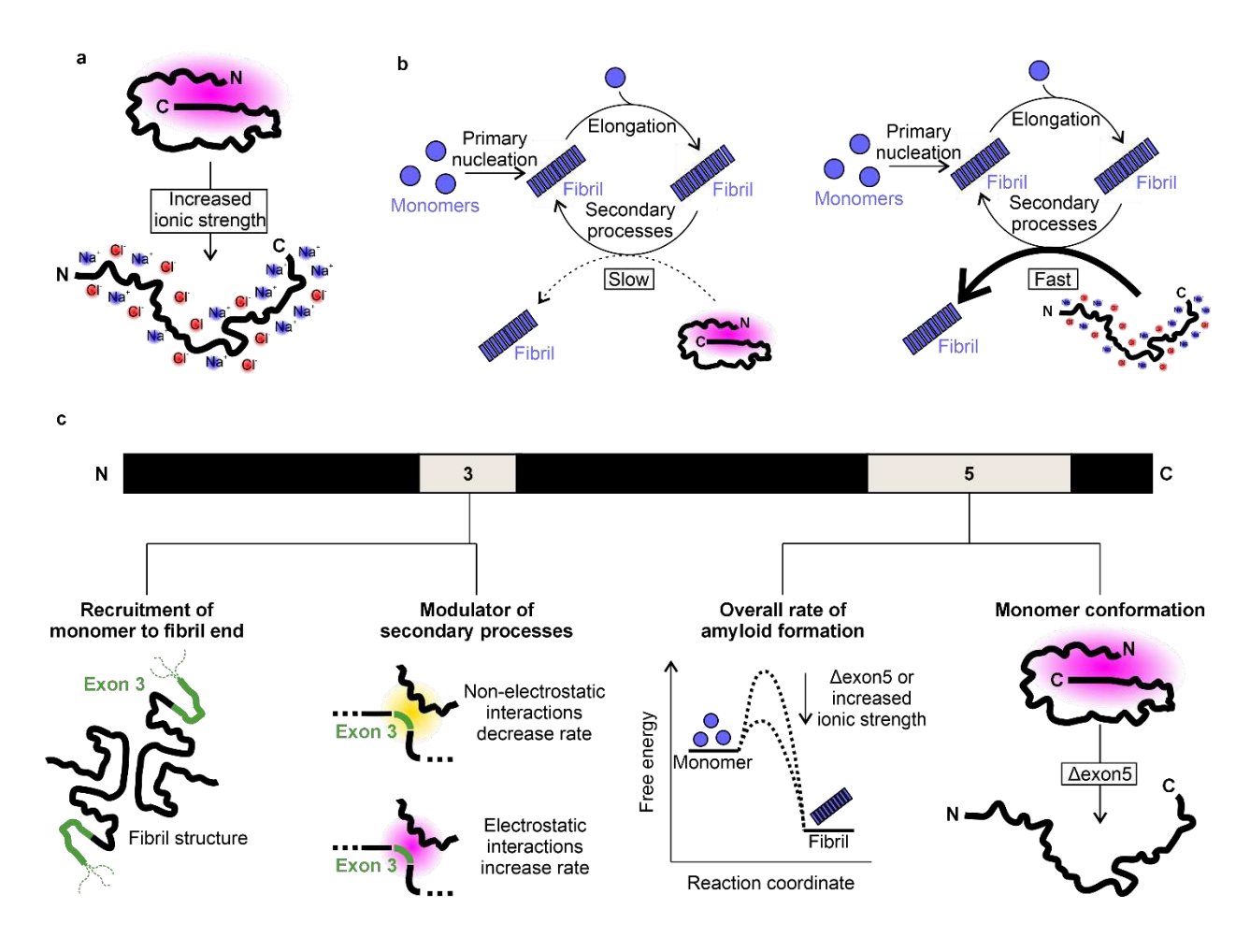


Figure 8. The importance of monomer conformation in amyloid formation of the alternative splice variants of  $\alpha Syn$ . (a) Under low ionic strength conditions, electrostatic interactions, particularly between the N- and C-terminal domains of  $\alpha Syn$  cause compaction of the monomer. As ionic strength increases, these electrostatic interactions are screened, facilitating monomer expansion. (b) Amyloid formation of  $\alpha Syn$  is achieved via primary nucleation from monomers, fibril elongation, and secondary nucleation. The more expanded monomers undergo secondary nucleation faster. (c) Summary of the findings on the roles of exons 3 and 5 in modulating the conformational ensembles of monomeric  $\alpha Syn$  and the effects on amyloid formation kinetics. Exon 3 is required in the fibril for the recruitment of  $\alpha SynFL$  monomers (Figure 3) and modulates the rate of secondary nucleation (Figure 4). Exon 5 regulates the overall rate of amyloid formation by protecting the NAC domain (Figure 2) and altering monomer shape and compaction (Figure 5).

We propose that the kinetic effects of changing ionic strength on amyloid formation of all four variants observed here occurs via a mechanism in which conformational changes in the monomer and/or fibril fuzzy coat result in a more amyloid-compatible conformations at higher ionic strength. The influence of ionic strength on the rates of amyloid formation by αSyn has been investigated previously<sup>9,78–83</sup>, and some studies have observed a reduction in secondary processes with increasing ionic strength<sup>78</sup>, or a low rate of secondary processes relative to primary nucleation<sup>61</sup>, in contrast to the observations presented here. Differences in pH<sup>79</sup> (which affects the rates of both elongation and secondary nucleation<sup>61</sup>), or whether the experiments were shaking or quiescent (affecting fragmentation and secondary nucleation rates) could rationalise these differences. While an increase in the rate of the secondary pathway (κ) is observed at increased ionic strength, it should also be noted that this is accompanied by a decrease in the rate of the primary pathway (λ) for αSynFL (Figure S5), which likely explains the discrepancies with previous reports. Our observation that expansion of αSyn correlates with accelerated amyloid formation, although supported by other work<sup>52</sup>, also contrasts with previous reports that have shown (using Zn<sup>2+</sup> binding and ion mobility mass spectrometry (IM-MS)) that compaction of αSyn by binding of metal ions is coupled with faster kinetics of amyloid formation<sup>77,84</sup>; suggesting that metal ion binding, sequence variants, and increasing NaCl concentrations differently affect the processes of amyloid formation. Hence, the nature of the local and global compaction appears crucial in determining the amyloid potential and pathways of αSyn aggregation. As such, the effect of ionic strength on the amyloid kinetics of  $\alpha$ Syn is highly context dependent.

537

538

539

540

541

542

543

544

545

546

547

548

549

550

551

552

553

554

555

556

557

558

559

We note that additional underlying factors may also contribute to the connection between ionic strength and amyloid formation kinetics. Indeed, changes in the ionic strength could also alter the properties of the fibril surface that catalyses the conversion of monomer to amyloid via

secondary nucleation. Some of the N-terminal region and most of the C-terminal domain of  $\alpha$ Syn are disordered in  $\alpha$ Syn amyloid fibril structures<sup>85</sup> and, given the high proportion of charged residues in these domains (Figure 1c), their conformational properties will likely also be altered by changes in ionic strength. Similarly, the influence of ionic strength on the colloidal properties of fibrils of the alternative splice variants of  $\alpha$ Syn remains unknown, and it is possible that changes in charge screening may alter the propensity for fibril-fibril interactions. Hence, changes in the fuzzy coat in response to ionic strength changes may contribute to the observed effects on the rate of secondary nucleation, by changing the catalytic site and/or by reducing the number of accessible sites on the fibril surface.

Our analysis using CALVADOS 2 also identified two key regions in the  $\alpha$ Syn sequence in which inter-residue distances strongly correlate with  $\kappa$ , suggesting that the local conformation of these regions affects the rate of secondary nucleation. Specifically, an expanded NAC and compact C-terminal domain are correlated with a high  $\kappa$ , and *vice versa*. This accords with proposals that exposure of the NAC region facilitates the transition to an amyloid state<sup>52</sup>, compaction of the residues at the C-terminus of  $\alpha$ Syn (e.g. at lower pH) is associated with an increase in amyloidogenicity<sup>53,86</sup>, and that the C-terminal domain exerts a modulating effect on NAC<sup>8,9</sup>. Since our data show that these changes specifically correlate with the rate of the *secondary* pathway (i.e. secondary nucleation and elongation), it appears that this enhanced activity lies in the effects on the structural conversion of monomers by fibrils, rather than primary nucleation itself. Although there are several residue pairs in NAC and the C-terminal domain that correlate strongly with  $\kappa$ , it is striking that the inter-residue distance that correlates most strongly with  $\kappa$  is Q79-E83, given the identification of the E83Q variant in a patient with DLB<sup>87,88</sup>. Similarly, the importance of the Glu at position 83 in amyloid formation kinetics was also recently demonstrated<sup>89</sup>. Biophysical

characterisation has revealed not only that the E83Q substitution causes a shift to more extended monomer conformations (as measured by IM-MS), but interactions specifically with Q79 are altered in this variant (as monitored by NMR chemical shift perturbations)<sup>88</sup>. Furthermore, the E83Q variant forms amyloid more rapidly than αSynWT, and amyloid fibrils of this disease variant are substantially shorter than those of αSynWT, consistent with an enhanced rate of secondary nucleation. Together the characterisation of the E83Q variant supports our proposal that the Q79-E83 residue pair, as well as other aspects of local conformation in the NAC and C-terminal regions, are important determinants of the rate of the secondary nucleation in amyloid formation.

## Roles of residues encoded by exons 3 and 5 in amyloid formation of αSyn

The results presented support previous studies that have shown that deletion of residues encoded by exon 5 accelerates amyloid formation of  $\alpha \text{Syn}^{47,49}$ , consistent with literature precedents that the C-terminal domain of  $\alpha \text{Syn}$  monomers can protect the hydrophobic core domain from amyloid formation<sup>8</sup>. Our results also show that residues in exon 3 ( $^{41}\text{GSKTKEGVVHGVAT}^{54}$ ) in the fibril are required for the recruitment of  $\alpha \text{SynFL}$  monomers in seeded fibril growth reactions, consistent with recently reported findings<sup>49</sup>. The finding that  $\alpha \text{Syn}\Delta 5$  is the only splice variant capable of cross-seeding  $\alpha \text{SynFL}$  monomers is surprising, given the proposed model that the N-terminal 11 amino acids of the monomer bind to the C-terminal domain in the fibril 'fuzzy coat'<sup>75,90</sup>, of which 28 residues are missing in the  $\alpha \text{Syn}\Delta 5$  variant (Figure 1). It has been noted previously that seeds with C-terminal truncations can indeed recruit  $\alpha \text{SynFL}$  monomers, albeit more slowly than self-seeding<sup>9</sup>. Instead, we find that it is residues 41-54 of the fibril that need to be present to facilitate efficient seeding of  $\alpha \text{Syn}$  monomers (Figure 3). Notably, these 14 residues are present in the fibril core in many of the >140  $\alpha \text{Syn}$  amyloid fibril structures<sup>63,85</sup>, which suggests

why  $\alpha SynFL$  is unable to adopt the fold of  $\alpha Syn\Delta 3$  amyloid via elongation. Furthermore, we note that proteinase K digestion of fibrils of  $\alpha SynFL$  and  $\alpha Syn\Delta 5$  suggest that they contain the same residues in the fibril core<sup>49</sup>. Although we do not have information on the fibril core structures of the alternative splice variants generated in this work, residues 103-130 are not resolved in any of the published amyloid fibril structures<sup>62,63</sup>, this ultimately allows us to rationalise why the deletion of these residues does not affect the ability of  $\alpha SynFL$  to adopt the fold of  $\alpha Syn\Delta 5$  amyloid fibrils in the process of elongation. Additionally, the involvement of the N-terminal residues of the fibril in seeded growth has been observed previously<sup>10</sup>, with truncated proteins  $\alpha Syn36-140$  and  $\alpha Syn41-140$  unable to recruit  $\alpha SynFL$  monomers. The implications of these findings in terms of PD pathogenesis are that if  $\alpha Syn\Delta 5$  is indeed capable of forming amyloid in the brain, that it may also have the capacity to recruit the more abundant  $\alpha SynFL$ , triggering the chain reaction of amyloid formation and subsequent cell-to-cell spreading of amyloid in disease.

# Conclusion

We have demonstrated that the higher propensity of  $\alpha Syn\Delta 5$  and  $\alpha Syn\Delta 3\Delta 5$  to form amyloid *in vitro* can be rationalised from differences in monomer conformations compared with  $\alpha SynFL$ , particularly global conformation in terms of prolateness, in addition to local conformation in the NAC and C-terminal regions and the extent to which the NAC is shielded by the rest of the protein sequence. Although the physiological and pathological importance of the  $\alpha Syn$  splice variants remains unknown, our findings suggest that the splice variants could be involved in disease pathogenesis, particularly  $\alpha Syn\Delta 5$ , which we have shown can recruit  $\alpha SynFL$  monomers via fibril elongation and to self-propagate most rapidly via secondary nucleation. If these variants do indeed prove to be involved in the pathogenesis of synucleinopathies, they might be targeted for disease

treatments; for example with RNA interference technology, which would be designed to target specific toxic isoforms of *SNCA* and facilitate cleavage of the relevant mRNA to prevent it from being translated<sup>91</sup>. This technology has already proved successful in reducing levels of another amyloidogenic protein, transthyretin, in familial amyloid polyneuropathy<sup>92</sup>.

From an evolutionary perspective, the sequence patterning that facilitates the promiscuous functions of  $\alpha \mathrm{Syn^{35}}$  has enabled the N- and C-terminal domains to mitigate aggregation driven by the NAC domain. Our results suggest that monomeric  $\alpha \mathrm{Syn}$  must exist in a carefully balanced equilibrium of conformations, where changes in sequence or modulation of the environmental conditions, probed here by changes in ionic strength, can critically determine its amyloidogenicity.

638

639

640

641

642

643

644

645

646

647

648

649

650

629

630

631

632

633

634

635

636

637

# **Experimental Section**

# Generation of plasmids

DNA plasmids designed for recombinant protein expression of the alternative splice variants were generated from the pET23a vector encoding αSyn (gifted by Professor Jean Baum, Department of Chemistry and Chemical Biology, Rutgers University, NJ, USA). To generate the  $\alpha Syn\Delta 3$  variant, primers were designed to facilitate deletion of amino acid residues <sup>41</sup>GSKTKEGVVHGVAT<sup>54</sup> by Q5 site-directed mutagenesis (NEB). Similarly, for generation of  $\alpha Syn\Delta 5$ , the primers designed for the deletion of residues were <sup>103</sup>NEEGAPQEGILEDMPVDPDNEAYEMPSE<sup>130</sup> from the αSynFL construct. To generate  $\alpha Syn\Delta 3\Delta 5$ , these latter primers were used on the  $\alpha Syn\Delta 3$  construct. Q5 site-directed mutagenesis was carried out using the primers (Table S15), subsequently followed by treatment with kinase, ligase and DpnI to facilitate DNA circularisation and template removal. Validation of the correct

deletion was achieved by transforming E. coli DH5 $\alpha$  cells, Miniprep (Qiagen), and DNA sequencing (Source Bioscience).

# Protein expression and purification

The plasmids generated above were used for the expression of recombinant protein of all variants of  $\alpha$ Syn. *E. coli* BL21 DE3 cells were transformed with the plasmid of interest by heatshock at 42 °C and bacteria grown on LB-agar plates containing carbenicillin (100 mg/mL) overnight at 37 °C. The following day, 100 mL carbenicillin-containing LB medium was inoculated with a single colony and incubated for ~16 h (overnight) at 37 °C 200 rpm. The next day, 15 mL starter culture was added per 1 L of LB medium (containing 100 mg/mL carbenicillin) and placed in an incubator (shaking at 200 rpm at 37 °C). Once the OD<sub>600</sub> reached ~0.6, 1 mM of isopropyl- $\beta$ -D-thio-galactopyranoside was added to induce expression of  $\alpha$ Syn protein. The cultures were placed back in the shaking incubators and left to express protein for 4-5 hours. After this time, the culture was centrifuged at 5,000 rpm (rotor JA 8.1) at 4 °C, and the cell pellet was stored at -20 °C until further use.

The cell pellets were thawed and homogenised in lysis buffer (20 mM Tris-HCl pH 8.0, 2 mM MgCl<sub>2</sub>, 5 mM DTT, 1 mM PMSF, 2 mM benzamidine, 100 μg/mL lysozyme, and 20 μg/mL DNase) and incubated on a roller at room temperature for 30 min. After this time, the homogenate was boiled at 80 °C for 10 min and subsequently centrifuged at 35,000 x g for 30 min. 30% (w/v) ammonium sulphate was then added to the resulting supernatant fraction and the sample was incubated on a roller at 4 °C to facilitate protein precipitation. The sample was then centrifuged again at 35,000 x g for 30 min at 4 °C, with the pelleted fraction retained afterwards. The

precipitation and centrifugation steps were repeated once more, and the resulting pellet was stored at -20 °C until further processing.

The sample was next purified by anion exchange chromatography. The pellet was thawed and resuspended in buffer A: 20 mM Tris-HCl (pH 8.0 for  $\alpha$ SynFL and  $\alpha$ Syn $\Delta$ 3, and pH 9.0 for  $\alpha$ Syn $\Delta$ 5 and  $\alpha$ Syn $\Delta$ 3 $\Delta$ 5 due to differences in the isoelectric points of the proteins). Anion exchange chromatography was carried out using a Q-Sepharose column packed in-house. Protein was applied to the column and washed with two column volumes (CV) of 20 mM Tris-HCl at the relevant pH. A gradient with buffer B (20 mM Tris-HCl, 1 M NaCl at pH 8.0 or 9.0 as above) was then applied to the column up to 50% ( $\nu$ / $\nu$ ) final concentration over two CVs. The same ratio of buffer A and B was applied to the column for an additional two CVs, before washing the column with 100% buffer B over two CVs. The eluted  $\alpha$ Syn proteins were then dialysed into 5 mM ammonium bicarbonate, lyophilised, and stored at -20 °C until further use.

The protein was next purified further using size exclusion chromatography on a HighLoad<sup>TM</sup>26-60 Superdex 75 prep grade gel filtration column. The lyophilised protein was first dissolved in phosphate-buffered saline (137 mM NaCl, 2.7 mM KCl, 8.1 mM Na<sub>2</sub>HPO<sub>4</sub> and 1.5 mM KH<sub>2</sub>PO<sub>4</sub>, pH 7.4) at a concentration of 2 mg/mL and injected onto the column in 5 mL loading volumes using a 50 mL Superloop. Collected protein was dialysed into 5 mM ammonium bicarbonate, lyophilised, and stored as described above. Correct and pure protein was confirmed using SDS PAGE and ESI-mass spectrometry.

## Thioflavin T assays

Lyophilised protein was dissolved in the buffers defined in the figure legends, centrifuged at 16,602 xg for 30 min at 4 °C to remove insoluble material. Protein concentration was determined

by measuring the  $A_{280}$  using an extinction coefficient ( $\epsilon$ ) of 5,960 M<sup>-1</sup> cm<sup>-1</sup> for  $\alpha SynFL$  and  $\alpha Syn\Delta 3$ , and  $\epsilon$  of 4,470 M<sup>-1</sup> cm<sup>-1</sup> for  $\alpha Syn\Delta 5$  and  $\alpha Syn\Delta 3\Delta 5$ . For the *de novo* ThT assays the protein at the concentration defined in the figure key was mixed with 20  $\mu$ M ThT and 100  $\mu$ L added to the assay plate (Corning – 3651) in triplicate. A single 3 mm Teflon polyball (PolySciences) was added to each well of the assay plate, which was subsequently placed in the FLUOstar Omega Plate Reader (BMG Labtech). The ThT assay was carried out at 37 °C for 45 h with orbital shaking (600 rpm). The fluorescence of each well of the plate was measured using an excitation wavelength of 444 nm with the emission monitored at 480 nm.

For the seeding ThT assays, the starting monomer concentration was 50 µM. The fibril seeds were prepared by taking the fibrils generated in the *de novo* ThT assay and subjecting them to two rounds of 30 sec sonication using a Cole-Parmer-Ultraprocessor sonicator and 40% power. The fibril seeds were added to the seeding experiments at a concentration of 5 µM (monomer equivalent). ThT assay was performed as above, in the absence of the Teflon polyball and with no shaking in the FLUOstar OPTIMA Plate Reader (BMG Labtech).

The  $T_{50}$  values for the ThT assays carried out at different monomer starting concentrations are defined as the first datapoint that crosses the threshold of 50% of the maximum ThT signal of the normalized curve. Values for the scaling exponent (Table S2) were determined by performing non-linear regression of the  $T_{50}$  values versus the starting concentration of  $\alpha$ Syn using the equation

$$y = ax^{\gamma}$$
 [1]

where a and  $\gamma$  are the scaling coefficient and exponent, respectively. Fitting and calculation of the 95% confidence intervals (CI) were carried out in GraphPad Prism 10.3.1.

For measurements of the ionic strength dependence of amyloid formation using ThT assays, the starting monomer protein concentration was 100  $\mu$ M. The ThT assays were carried out as described above for the *de novo* experiments.

ThT data from the ionic strength dependence experiment were fitted to the equation<sup>64</sup>

$$y = 1 - \left[1 + \frac{\lambda^2}{2\kappa^2 \theta} e^{\kappa t}\right]^{-\theta}$$
 [2]

where y = normalised ThT intensity, t = time, and  $\lambda$ ,  $\kappa$  and  $\theta$  are fitted parameters with  $0 \le \theta \le$  3.  $\lambda$  and  $\kappa$  were fitted for each replicate, but  $\theta$  was fitted globally for each variant. Note that only data prior to the maximum fluorescence value was used for fitting, this is to account for the decreases in signal observed during the plateau, particularly for  $\alpha \text{Syn}\Delta 5$  and  $\alpha \text{Syn}\Delta 3\Delta 5$ , which is potentially due to flocculation and is not accounted for in current models of amyloid formation.

To test whether fragmentation is the dominant secondary process in our experiments, we first performed a ThT assay using 100  $\mu$ M monomer in 20 mM sodium phosphate, 100 mM NaCl, pH 7.4 at 37 °C under orbital shaking at 600 rpm in the presence of a Teflon bead. At 30 h we collected the fibrils and added these (without sonicating) to fresh monomer of the same variant (50  $\mu$ M monomer plus 10  $\mu$ M monomer equivalent concentration of seed). The kinetics of self-seeding was assessed as described for the seeding assays described above. 15 h later (45 h after the start of the first *de novo* ThT assay), we collected fibrils from another well and tested the self-seeding potential again.

If fragmentation is the dominant secondary process in *de novo* fibril self-assembly, there is a precise expected relationship between  $\kappa$  and the rate of change of the seeding potency of a plateauphase fibril sample due to fragmentation. In elongation-dominated seeding, monomer disappears exponentially at a rate dependent on the seed fibril number concentration  $P_{\text{seed}}$  and elongation rate constant  $k_{+}^{94}$ .

$$m(t) = m_0 e^{-kt} \,, ag{3a}$$

$$k = 2k_{+}P_{\text{seed}}, \qquad [3b]$$

where m(t) is the monomer concentration as a function of time, and  $m_0$  is the initial monomer concentration in the seeded assay. This rate of disappearance can be influenced by incubating the fibrils for longer before use, allowing them to fragment more. After a time delay  $\Delta t$ , the concentration of fibril ends will have increased by an amount proportional to the fragmentation rate  $k_{\text{frag}}$  and seed fibril mass  $M_{\text{seed}}^{94}$ .

$$P_{\text{seed}} = P_{\text{seed}} + k_{\text{frag}} M_{\text{seed}} \Delta t .$$
 [4]

- This means that, if fragmentation occurs at a significant rate, a fibril sample that has been incubated for longer before use will have more fibril ends and thus greater self-seeding potency.
- We can quantify this effect by combining equations [3] and [4],

758

759

760

761

$$k' = k + 2k_{\text{frag}}k_{+}M_{\text{seed}}\Delta t.$$
 [5]

If fragmentation is also the dominant secondary process in *de novo* fibril self-assembly, then  $\kappa^2 = 2k_{\text{frag}}k_+m_{\text{original}}, \text{ where } m_{\text{original}} \text{ is the original monomer concentration used to assemble}$ the seed fibrils before use in the seeded assay. This means there will be a direct link between  $\kappa$  and the effect of fragmentation on k,

$$k' = k + \kappa^2 r \Delta t \,, \tag{6a}$$

$$r = \frac{M_{\text{seed}}}{m_{\text{original}}}.$$
 [6b].

However, equation [6] holds only if fragmentation is the dominant secondary process in *de novo* fibril assembly. If fragmentation is not the dominant secondary process, k' will be smaller than the measured value of  $\kappa$  would predict, or conversely  $\kappa$  will be too large to be explained by the change from k to k' alone.

We globally fitted the fluorescence intensity changes over time from three replicates to an exponential decay,

764 
$$y = a(1 - e^{-kt})$$
 [7]

where y is the normalised ThT intensity, t is time, a is the amplitude of the exponential fit, and k is the rate constant. Equation [7] is simply a transformation of equation [3a], and their rate constants have the same meaning. Theoretical predictions of k' were then calculated using equation [6], where k' is the predicted rate constant at t = 45 h if fragmentation were the dominant secondary process,  $\kappa$  is fitted from the corresponding de novo ThT assay, r is the seed dilution factor (0.1), and  $\Delta t$  is the time interval between the first and second seeding reactions (i.e. 15 h). In all cases where this was performed, the observed k' was much less than the predicted k', indicating that fragmentation cannot be the dominant secondary process in de novo assembly.

#### Mathematical models of the effect of ionic strength on $\kappa$

Extracted values of  $\kappa$  at varying ionic strength were fitted to two mathematical models describing possible effects of ionic strength on the rate of secondary nucleation. We considered two possible scenarios: the 'Free Energy Barrier' model, in which ions screen out an unfavourable electrostatic term in the free energy barrier for secondary nucleation; and the 'Brønsted-Bjerrum' model, in which ions affect the rate by altering the activity of the precursor(s) of secondary nucleation. As described in (Derivations), the 'Free Energy Barrier' model predicts saturation of  $\kappa$  at high ionic strength according to the relation,

$$\kappa = \kappa_{\text{sat}} \left(\frac{\kappa_0}{\kappa_{\text{sat}}}\right)^{2^{-\sqrt{I/I_{\text{mid}}}}}$$
 [8]

where  $\kappa_0$  and  $\kappa_{\rm sat}$  are the limits of  $\kappa$  at low and high ionic strength, respectively, and  $I_{\rm mid}$  is the ionic strength at which a midpoints is reached. Precise definitions are given in (Derivations). On the other hand, the 'Brønsted-Bjerrum' model has a lower limit  $\kappa_0$  but no saturation,

$$\kappa = \kappa_0 2^{\sqrt{\frac{I}{I_2}}}$$
 [9]

where  $I_2$  is the ionic strength at which there is a two-fold enhancement of  $\kappa$  relative to  $\kappa_0$ , and the definitions of  $\kappa_0$  and  $I_2$  are again given in (Derivations). Crucially, while eq. [8] predicts saturation of  $\kappa$  at high ionic strength, eq. [9] does not.

The 'Free Energy Barrier' model is equivalent to stabilisation of the critical nucleus of secondary nucleation, or an equivalent charged transition state in fragmentation, by electric field screening according to Debye-Hückel theory. The 'Brønsted-Bjerrum' model is equivalent to stabilisation of a secondary nucleation intermediate prior to the critical nucleus, i.e. reduced electrostatic repulsion between the monomers and the fibril surface.

To compare the ability of the models to describe the variation of  $\kappa$  with ionic strength, both models were fitted to values of  $\kappa$  extracted using eq. [2] at different ionic strengths, and the quality of the fits was assessed using Akaike's corrected information criterion (AICc). For the 'Free Energy Barrier' model, the fitted parameters were  $\kappa_0$ ,  $\kappa_{\rm sat}$ , and  $I_{\rm mid}$ . For the 'Brønsted-Bjerrum' model, the fitted parameters were  $\kappa_0$  and  $I_2$ . Fitting was performed in GraphPad Prism 10.4.2 using Levenberg-Marquardt non-linear least-squares regression.

## Pelleting assay

A pelleting assay was used to determine the percentage of protein converted into insoluble material at the end of the ThT assays. Immediately following the end of the ThT assays, samples were retrieved from the assay plates and centrifuged at 100,000 xg for 30 min at 4 °C. The

supernatant and whole fractions were loaded onto 15% Tris-tricine SDS-PAGE gels. The gels were subsequently stained with InstantBlue Coomassie stain and the densitometry of the bands measured using Nine-Alliance software. The percentage of pelletable material was determined using the equation:

811 
$$Percentage \ pelletable = 100 \times 1 - \left(\frac{D_{sol}}{D_{whole}}\right)$$
 [10]

where  $D_{sol}$  is the densitometry of the soluble fraction and  $D_{whole}$  is the densitometry of the whole sample. The pelleting assay was performed three times.

# Negative stain transmission electron microscopy

Negative stain transmission electron microscopy (TEM) was carried out on the end products of the ThT assays. The samples were administered to carbon-coated copper grids, which was subsequently washed three times with 18 M $\Omega$  H<sub>2</sub>O and strained with 2% (w/v) uranyl acetate. Imaging was performed with a FEI Tecnai T12 electron microscope.

# Flow induced dispersion analysis (FIDA)

Flow induced dispersion analysis (FIDA) was performed on a Fida-1 instrument (FidaBio) with a 75 μm x 1 m capillary. The capillary was washed with 1 M NaOH and coated with HS reagent (FidaBio), with distilled water between and after. Monomeric protein was dissolved in 20 mM sodium phosphate buffer at pH 7.4 in the absence of NaCl, at a protein concentration of 400 μM. Analysis runs were carried out in the same buffer with the desired concentration of NaCl, as the small plug of sample (~50 nL) rapidly disperses into the NaCl-containing buffer after injection onto the capillary. Each FIDA run had 3 steps: (1) equilibration with buffer for 90 s at 3500 mbar; (2) injection of a plug of sample for 10 s at 50 mbar; and (3) elution with further blank for 3 min

at 400 mbar. The elution of protein was monitored by intrinsic fluorescence (excitation 275 nm, emission 300-450 nm) and the hydrodynamic radius was calculated from the baseline-subtracted Taylorgram using the FIDA analysis software (FidaBio).

833

834

835

836

837

838

839

840

841

842

843

844

845

846

847

848

849

850

851

830

831

832

#### Molecular dynamics (MD) simulations

All coarse-grained MD simulations were performed using the CALVADOS 2 force field<sup>57,58</sup>. Simulations were performed as stated previously<sup>57,58</sup>, except for differences in box size and simulation duration as stated below. In short, CALVADOS uses a simplified representation of one bead per residue, connected by harmonic bonds with an equilibrium distance of 0.38 nm and force constant of 8033 kJ.mol<sup>-1</sup>.nm<sup>-2</sup>. Molecular interactions between non-adjacent beads are accounted for by additional potentials: a truncated and shifted Ashbaugh-Hatch potential for non-electrostatic interactions, and a truncated Debye-Hückel potential for electrostatic interactions. Ionic strength is accounted for by changes in the Debye length used to model electrostatic interactions 57,58. At the start of each simulation, a single αSyn monomer was initialised as a linear polymer with beads separated by 0.38 nm in a periodic box of size 0.76(N-1) + 4 nm, where N is the number of beads. Simulations were carried out using a Langevin integrator with a timestep of 10 fs and friction coefficient of 0.01 ps<sup>-1</sup>, with a sampling frequency of 70 ps (7000 timesteps) per frame, which yields weakly correlated frames<sup>58</sup>. After an initial equilibration of 700 ps (7 x 10<sup>4</sup> timesteps), the simulation was carried out for 350 ns (35 x 106 timesteps) to obtain 5000 frames sampling the protein's simulated conformational landscape. All simulations were carried out at 310 K, pH 7.4 at the ionic strengths indicated in the text. The structural parameters  $R_g$ , v,  $\Delta$ , and S and their errors were calculated as described in <sup>58</sup>.

To classify  $\alpha$ Syn conformers by spectral clustering, we first calculated the pairwise similarity (affinity) of each pair of frames in a simulation. We chose to compare inter-residue  $C_{\alpha}$ - $C_{\alpha}$  distances rather than aligned  $C_{\alpha}$  coordinates, as inter-residue distances preserve information about structural contacts in spite of the large continuous deformations typically seen in CALVADOS 2 simulations of IDRs. The affinity score  $A_{xy}$  each pair of frames (x, y) was calculated as the Gaussian kernel of the mean squared deviation in inter-residue  $(C_{\alpha}$ - $C_{\alpha}$ ) distances between the two frames, using the mean expected squared deviation in inter-residue distances as the normalisation. Specifically,

859 
$$A_{xy} = \exp\left[-\frac{\langle \Delta d_{ij}^2 \rangle}{\langle \mathbb{E}(\Delta d_{ij}^2) \rangle}\right], \quad [11]$$

where  $\langle ... \rangle = \sum_{i>j+1} .../N$  represents an average across all N non-bonded residue pairs (i,j),  $\Delta d_{ij}^2 = \left(d_{ij,x} - d_{ij,y}\right)^2$  is the squared deviation in inter-residue distance  $d_{ij}$  between frames x and y, and  $\mathbb{E}(\Delta d_{ij}^2) = 2 \mathrm{Var}(d_{ij})$  is the expected squared deviation in  $d_{ij}$  for a randomly chosen pair of independent and identically distributed frames. Note that the mean across residue pairs  $\langle ... \rangle$  was taken separately on the numerator and denominator to preserve a stronger weighting for residue pairs that experience large variations throughout the simulation trajectory. As a result,  $A_{xy}$  is essentially a Gaussian transformation of the Euclidean distance between frames in the higher-dimensional  $(d_{13} ... d_{R-2,R})$  space, for a sequence of R residues. We then used the resulting affinity matrix A to classify frames into 4 clusters using the SpectralClustering class in scikit-learn<sup>93</sup>. Alternative numbers of clusters provided similar results, but were less interpretable as they failed to separately resolve intra-domain and long-range interactions. Note that we do not claim that these clusters represent distinct basins in the conformational free energy landscape of  $\alpha$ Syn, which appears to be continuous in CALVADOS 2 simulations. Instead, the spectral clustering algorithm provides a means to carve up the conformational spectrum of  $\alpha$ Syn into closely related states. The

increase in the population of the compact class with exon 5 present, therefore, likely reflects the skewing of the conformational distribution to produce an enhanced population of closely interrelated compact states. As clustering was carried out independently for each variant, the compact classes of different variants are not necessarily the same; however, inspection of the per-cluster contact maps showed the same pattern of N-C interactions in each case.

# **Corresponding Authors**

\*for correspondence: S.E.Radford@leeds.ac.uk and D.J.Brockwell@leeds.ac.uk

# Data availability

The data supporting the findings of this study are available from https://doi.org/10.5518/1695.

# **Supporting Information**

Tables showing summary of mRNA expression levels of the alternative splice variants of  $\alpha$ Syn in disease,  $T_{50}$  values, scaling exponents, AmyloFit fitted parameters, and insoluble protein yield for the ThT assay at different starting monomer concentrations, insoluble protein yields from cross-seeding experiment, sequence properties of the alternative splice variants of  $\alpha$ Syn, fitted values  $(\lambda \kappa/\theta)$  and insoluble protein yield for the ionic strength ThT assay, comparison between the 'Brønsted-Bjerrum' and 'Free Energy Barrier' models, fitted values from the 'Free Energy Barrier' model,  $R_h$  values of the alternative splice variants of  $\alpha$ Syn at different added NaCl concentrations, CALVADOS 2 predicted  $R_g$  values, and chain-length independent measures of the alternative splice variants of  $\alpha$ Syn at different ionic strengths, primers used in this work.

Supplementary figures showing fitted models from AmyloFit, *de novo* amyloid kinetics of  $\alpha Syn\Delta 5$  and  $\alpha Syn\Delta 3\Delta 5$  at low starting monomer concentration, self-seeding kinetics, yield, and negative-stain images, fitted curves for the ThT assays at different ionic strengths, fitted  $\lambda$  values, confidence ellipses from  $\lambda$  and  $\kappa$  fitting, elongation-dominated self-seeding at different points in the plateau phase, attempts to fit the  $\kappa$  values using the Brønsted-Bjerrum equation, representative Taylorgrams, contact probability maps, contact probability difference maps, spectral clustering probability distributions, proportion of clustering frames across ionic strengths, representative conformations with different  $\Delta$  and S values, correlations of ranked data, Spearman's rank heatmap of inter-residue distances, derivations of the 'Free Energy Barrier' and 'Brønsted-Bjerrum' models of the effect of ionic strength on  $\kappa$ .

## Acknowledgments

We thank all members of the Radford and Brockwell labs for helpful discussions, and Nasir Khan for excellent technical support. We also thank Leon Willis for help with multivariate analyses. Negative stain TEM images were collected using facilities in the Astbury Biostructure Laboratory and was funded by the University of Leeds and Wellcome (094232/Z/10/Z). FIDA data were collected on a Fida One, which was funded by the BBSRC (BB/Z516053/1). KMD is funded by MRC (MR/N013840/1) and Wellcome (204963), AIPT is funded by Wellcome (204963). S.E.R. holds a Royal Society Professorial Fellowship (RSRP/R1/211057).

## **Abbreviations**

AICc, Akaike's corrected information criterion;  $\alpha$ Syn,  $\alpha$ -synuclein;  $\alpha$ SynFL,  $\alpha$ -synuclein full-length; CV, column volume; DLB, Dementia with Lewy bodies; FIDA, flow-induced

dispersion analysis; IM-MS, ion mobility mass spectrometry; MD, molecular dynamics; MSA, Multiple System Atrophy; NAC, non-amyloid  $\beta$  component; PD, Parkinson's disease;  $R_g$ , radius of gyration;  $R_h$ , hydrodynamic radius; SEM, standard error of the mean; TEM, transmission electron microscopy; ThT, thioflavin T

## 924 References

- 925 (1) Koga, S.; Sekiya, H.; Kondru, N.; Ross, O. A.; Dickson, D. W. Neuropathology and Molecular Diagnosis of Synucleinopathies. *Mol. Neurodegener.* **2021**, *16* (1), 83. https://doi.org/10.1186/s13024-021-00501-z.
- Arima, K.; Uéda, K.; Sunohara, N.; Hirai, S.; Izumiyama, Y.; Tonozuka-Uehara, H.; Kawai,
   M. Immunoelectron-Microscopic Demonstration of NACP/α-Synuclein-Epitopes on the
   Filamentous Component of Lewy Bodies in Parkinson's Disease and in Dementia with Lewy
   Bodies. *Brain Res.* 1998, 808 (1), 93–100. https://doi.org/10.1016/S0006-8993(98)00734-3.
- 932 (3) Mezey, E.; Dehejia, A. M.; Harta, G.; Suchy, S. F.; Nussbaum, R. L.; Brownstein, M. J.; 933 Polymeropoulos, M. H. Alpha Synuclein Is Present in Lewy Bodies in Sporadic Parkinson's Disease. *Mol. Psychiatry* **1998**, *3* (6), 493–499. https://doi.org/10.1038/sj.mp.4000446.
- 935 (4) Takeda, A.; Mallory, M.; Sundsmo, M.; Honer, W.; Hansen, L.; Masliah, E. Abnormal Accumulation of NACP/Alpha-Synuclein in Neurodegenerative Disorders. *Am. J. Pathol.* 1998, *152* (2), 367–372.
- 938 (5) Otzen, D. E. Antibodies and α-Synuclein: What to Target against Parkinson's Disease?
  939 Biochim. Biophys. Acta BBA Proteins Proteomics 2024, 1872 (2), 140943.
  940 https://doi.org/10.1016/j.bbapap.2023.140943.
- Flagmeier, P.; Meisl, G.; Vendruscolo, M.; Knowles, T. P. J.; Dobson, C. M.; Buell, A. K.;
   Galvagnion, C. Mutations Associated with Familial Parkinson's Disease Alter the Initiation
   and Amplification Steps of α-Synuclein Aggregation. *Proc. Natl. Acad. Sci. U. S. A.* 2016,
   113 (37), 10328–10333. https://doi.org/10.1073/pnas.1604645113.
- 945 (7) Stephens, A. D.; Zacharopoulou, M.; Moons, R.; Fusco, G.; Seetaloo, N.; Chiki, A.; Woodhams, P. J.; Mela, I.; Lashuel, H. A.; Phillips, J. J.; De Simone, A.; Sobott, F.; Schierle, G. S. K. Extent of N-Terminus Exposure of Monomeric Alpha-Synuclein Determines Its Aggregation Propensity. *Nat. Commun.* 2020, 11 (1), 2820. https://doi.org/10.1038/s41467-020-16564-3.
- (8) Farzadfard, A.; Pedersen, J. N.; Meisl, G.; Somavarapu, A. K.; Alam, P.; Goksøyr, L.; Nielsen,
   M. A.; Sander, A. F.; Knowles, T. P. J.; Pedersen, J. S.; Otzen, D. E. The C-Terminal Tail of
   α-Synuclein Protects against Aggregate Replication but Is Critical for Oligomerization.
   Commun. Biol. 2022, 5 (1), 1–10. https://doi.org/10.1038/s42003-022-03059-8.
- Wateren, I. M. van der; Knowles, T. P. J.; Buell, A. K.; Dobson, C. M.; Galvagnion, C. C Terminal Truncation of α-Synuclein Promotes Amyloid Fibril Amplification at Physiological
   pH. Chem. Sci. 2018, 9 (25), 5506–5516. https://doi.org/10.1039/C8SC01109E.
- 957 (10) McGlinchey, R. P.; Ni, X.; Shadish, J. A.; Jiang, J.; Lee, J. C. The N Terminus of α-Synuclein 958 Dictates Fibril Formation. *Proc. Natl. Acad. Sci.* **2021**, *118* (35), e2023487118. 959 https://doi.org/10.1073/pnas.2023487118.
- 960 (11) Den Hartog Jager, W. A. Sphingomyelin in Lewy Inclusion Bodies in Parkinson's Disease. 961 *Arch. Neurol.* **1969**, *21* (6), 615–619. 962 https://doi.org/10.1001/archneur.1969.00480180071006.

- Gai, W. P.; Yuan, H. X.; Li, X. Q.; Power, J. T. H.; Blumbergs, P. C.; Jensen, P. H. *In Situ* and *in Vitro* Study of Colocalization and Segregation of α-Synuclein, Ubiquitin, and Lipids in Lewy Bodies. *Exp. Neurol.* 2000, 166 (2), 324–333. https://doi.org/10.1006/exnr.2000.7527.
- 966 (13) Shahmoradian, S. H.; Lewis, A. J.; Genoud, C.; Hench, J.; Moors, T. E.; Navarro, P. P.; 967 Castaño-Díez, D.; Schweighauser, G.; Graff-Meyer, A.; Goldie, K. N.; Sütterlin, R.; 968 Huisman, E.; Ingrassia, A.; Gier, Y. de; Rozemuller, A. J. M.; Wang, J.; Paepe, A. D.; Erny, 969 J.; Staempfli, A.; Hoernschemeyer, J.; Großerüschkamp, F.; Niedieker, D.; El-Mashtoly, S. 970 F.; Quadri, M.; Van IJcken, W. F. J.; Bonifati, V.; Gerwert, K.; Bohrmann, B.; Frank, S.; Britschgi, M.; Stahlberg, H.; Van de Berg, W. D. J.; Lauer, M. E. Lewy Pathology in 971 972 Parkinson's Disease Consists of Crowded Organelles and Lipid Membranes. Nat. Neurosci. 973 **2019**, 22 (7), 1099–1109. https://doi.org/10.1038/s41593-019-0423-2.
- 974 (14) Trinkaus, V. A.; Riera-Tur, I.; Martínez-Sánchez, A.; Bäuerlein, F. J. B.; Guo, Q.; Arzberger,
  975 T.; Baumeister, W.; Dudanova, I.; Hipp, M. S.; Hartl, F. U.; Fernández-Busnadiego, R. In Situ
  976 Architecture of Neuronal α-Synuclein Inclusions. *Nat. Commun.* 2021, 12 (1), 2110.
  977 https://doi.org/10.1038/s41467-021-22108-0.
- 978 (15) Galvagnion, C.; Buell, A. K.; Meisl, G.; Michaels, T. C. T.; Vendruscolo, M.; Knowles, T. P.
   979 J.; Dobson, C. M. Lipid Vesicles Trigger α-Synuclein Aggregation by Stimulating Primary
   980 Nucleation. *Nat. Chem. Biol.* 2015, 11 (3), 229–234. https://doi.org/10.1038/nchembio.1750.
- 981 (16) Hellstrand, E.; Nowacka, A.; Topgaard, D.; Linse, S.; Sparr, E. Membrane Lipid Co 982 Aggregation with α-Synuclein Fibrils. PLOS ONE 2013, 8 (10), e77235.
   983 https://doi.org/10.1371/journal.pone.0077235.
- 984 (17) Doherty, C. P. A.; Ulamec, S. M.; Maya-Martinez, R.; Good, S. C.; Makepeace, J.; Khan, G.
  985 N.; van Oosten-Hawle, P.; Radford, S. E.; Brockwell, D. J. A Short Motif in the N-Terminal
  986 Region of α-Synuclein Is Critical for Both Aggregation and Function. *Nat. Struct. Mol. Biol.*987 2020, 27 (3), 249–259. https://doi.org/10.1038/s41594-020-0384-x.
- Ulamec, S. M.; Maya-Martinez, R.; Byrd, E. J.; Dewison, K. M.; Xu, Y.; Willis, L. F.; Sobott,
  F.; Heath, G. R.; van Oosten Hawle, P.; Buchman, V. L.; Radford, S. E.; Brockwell, D. J.
  Single Residue Modulators of Amyloid Formation in the N-Terminal P1-Region of α-Synuclein. *Nat. Commun.* 2022, *13* (1), 4986. https://doi.org/10.1038/s41467-022-32687-1.
- (19) Dewison, K. M.; Rowlinson, B.; Machin, J. M.; Crossley, J. A.; Thacker, D.; Wilkinson, M.;
  Ulamec, S. M.; Khan, G. N.; Ranson, N. A.; van Oosten-Hawle, P.; Brockwell, D. J.; Radford,
  S. E. Residues 2 to 7 of α-Synuclein Regulate Amyloid Formation via Lipid-Dependent and
  Lipid-Independent Pathways. *Proc. Natl. Acad. Sci. USA* 2024, *121* (34), e2315006121.
  https://doi.org/10.1073/pnas.2315006121.
- (20) Ghosh, D.; Torres, F.; Schneider, M. M.; Ashkinadze, D.; Kadavath, H.; Fleischmann, Y.;
  Mergenthal, S.; Güntert, P.; Krainer, G.; Andrzejewska, E. A.; Lin, L.; Wei, J.; Klotzsch, E.;
  Knowles, T.; Riek, R. The Inhibitory Action of the Chaperone BRICHOS against the α-Synuclein Secondary Nucleation Pathway. Nat. Commun. 2024, 15 (1), 10038.
  https://doi.org/10.1038/s41467-024-54212-2.
- (21) Burmann, B. M.; Gerez, J. A.; Matečko-Burmann, I.; Campioni, S.; Kumari, P.; Ghosh, D.;
  Mazur, A.; Aspholm, E. E.; Šulskis, D.; Wawrzyniuk, M.; Bock, T.; Schmidt, A.; Rüdiger, S.
  G. D.; Riek, R.; Hiller, S. Regulation of α-Synuclein by Chaperones in Mammalian Cells.
  Nature 2020, 577 (7788), 127–132. https://doi.org/10.1038/s41586-019-1808-9.

- (22) Gialama, D.; Vadukul, D. M.; Thrush, R. J.; Radford, S. E.; Aprile, F. A. A Potent Sybody
   Selectively Inhibits α-Synuclein Amyloid Formation by Binding to the P1 Region. J. Med.
   Chem. 2024, 67 (12), 9857–9868. https://doi.org/10.1021/acs.jmedchem.3c02408.
- (23) Nielsen, J.; Pedersen, J. N.; Kleijwegt, G.; Nowak, J. S.; Nami, F.; Johansen, C.; Sassetti, E.; 1009 1010 Berg, B. B.; Lyngsø, N. M.; Brøchner, B. V.; Carlson, J. H.; Simonsen, A.; Olsen, W. P.; 1011 Simonsen, B. W.; Mikkelsen, J. H.; Sereika-Bejder, V.; Aarup Lauritsen, J.; Merrild, K. F.; Malle, M. G.; Valero, J.; Kjems, J.; Bøggild, A.; Boesen, T.; Birkelund, S.; Christiansen, G.; 1012 Hansen, S. B.; Kristensen, M.; Madsen, P. S.; Strømgaard, K.; Romero-Ramos, M.; 1013 1014 Gustafsen, C.; Glerup, S.; Andersen, K. R.; Clausen, M. H.; Otzen, D. E. Nanobodies Raised 1015 against the Cytotoxic α-Synuclein Oligomer Are Oligomer-Specific and Promote Its Cellular Uptake. Npj Biosensing 2025, 2 (1), 23. https://doi.org/10.1038/s44328-025-00042-1. 1016
- (24) Santos, J.; Cuellar, J.; Pallarès, I.; Byrd, E. J.; Lends, A.; Moro, F.; Abdul-Shukkoor, M. B.;
  Pujols, J.; Velasco-Carneros, L.; Sobott, F.; Otzen, D. E.; Calabrese, A. N.; Muga, A.;
  Pedersen, J. S.; Loquet, A.; Valpuesta, J. M.; Radford, S. E.; Ventura, S. A Targetable N-Terminal Motif Orchestrates α-Synuclein Oligomer-to-Fibril Conversion. *J. Am. Chem. Soc.*2024, 146 (18), 12702–12711. https://doi.org/10.1021/jacs.4c02262.
- 1022 (25) Eliezer, D.; Kutluay, E.; Bussell, R.; Browne, G. Conformational Properties of α-Synuclein in Its Free and Lipid-Associated States. *J. Mol. Biol.* **2001**, *307* (4), 1061–1073. https://doi.org/10.1006/jmbi.2001.4538.
- 1025 (26) Ulmer, T. S.; Bax, A.; Cole, N. B.; Nussbaum, R. L. Structure and Dynamics of Micelle-1026 Bound Human α-Synuclein. *J. Biol. Chem.* **2005**, 280 (10), 9595–9603. 1027 https://doi.org/10.1074/jbc.M411805200.
- 1028 (27) Fouke, K. E.; Wegman, M. E.; Weber, S. A.; Brady, E. B.; Román-Vendrell, C.; Morgan, J. R. Synuclein Regulates Synaptic Vesicle Clustering and Docking at a Vertebrate Synapse. *Front. Cell Dev. Biol.* **2021**, *9*, 774650. https://doi.org/10.3389/fcell.2021.774650.
- 1031 (28) Logan, T.; Bendor, J.; Toupin, C.; Thorn, K.; Edwards, R. H. α-Synuclein Promotes Dilation 1032 of the Exocytotic Fusion Pore. *Nat. Neurosci.* **2017**, *20* (5), 681–689. https://doi.org/10.1038/nn.4529.
- 1034 (29) Lautenschläger, J.; Kaminski, C. F.; Kaminski Schierle, G. S. α-Synuclein Regulator of Exocytosis, Endocytosis, or Both? *Trends Cell Biol.* **2017**, *27* (7), 468–479. https://doi.org/10.1016/j.tcb.2017.02.002.
- 1037 (30) Goedert, M.; Griesinger, C.; Outeiro, T. F.; Riek, R.; Schröder, G. F.; Spillantini, M. G. 1038 Abandon the NAC in α-Synuclein. *Lancet Neurol.* **2024**, 23 (7), 669. https://doi.org/10.1016/S1474-4422(24)00176-5.
- (31) Giasson, B. I.; Murray, I. V. J.; Trojanowski, J. Q.; Lee, V. M.-Y. A Hydrophobic Stretch of
   1041 12 Amino Acid Residues in the Middle of α-Synuclein Is Essential for Filament Assembly. J.
   1042 Biol. Chem. 2001, 276 (4), 2380–2386. https://doi.org/10.1074/jbc.M008919200.
- (32) Binolfi, A.; Rasia, R. M.; Bertoncini, C. W.; Ceolin, M.; Zweckstetter, M.; Griesinger, C.; 1043 1044 Jovin, T. M.; Fernández, C. O. Interaction of α-Synuclein with Divalent Metal Ions Reveals 1045 Key Differences: A Link between Structure, Binding Specificity and Fibrillation 1046 Enhancement. Am. Chem. Soc. 2006, 128 (30),9893-9901. J. https://doi.org/10.1021/ja0618649. 1047

- (33) Lautenschläger, J.; Stephens, A. D.; Fusco, G.; Ströhl, F.; Curry, N.; Zacharopoulou, M.;
  Michel, C. H.; Laine, R.; Nespovitaya, N.; Fantham, M.; Pinotsi, D.; Zago, W.; Fraser, P.;
  Tandon, A.; St George-Hyslop, P.; Rees, E.; Phillips, J. J.; De Simone, A.; Kaminski, C. F.;
  Schierle, G. S. K. C-Terminal Calcium Binding of α-Synuclein Modulates Synaptic Vesicle
  Interaction. *Nat. Commun.* 2018, 9 (1), 712. https://doi.org/10.1038/s41467-018-03111-4.
- 1053 (34) Burré, J.; Sharma, M.; Tsetsenis, T.; Buchman, V.; Etherton, M. R.; Südhof, T. C. α-Synuclein 1054 Promotes SNARE-Complex Assembly in Vivo and in Vitro. *Science* **2010**, *329* (5999), 1663– 1667. https://doi.org/10.1126/science.1195227.
- 1056 (35) Longhena, F.; Faustini, G.; Spillantini, M. G.; Bellucci, A. Living in Promiscuity: The Multiple Partners of Alpha-Synuclein at the Synapse in Physiology and Pathology. *Int. J. Mol. Sci.* **2019**, *20* (1), 141. https://doi.org/10.3390/ijms20010141.
- 1059 (36) Goedert, M.; Eisenberg, D. S.; Crowther, R. A. Propagation of Tau Aggregates and Neurodegeneration. *Annu. Rev. Neurosci.* **2017**, 40 (1), 189–210. https://doi.org/10.1146/annurev-neuro-072116-031153.
- 1062 (37) Jarrett, J. T.; Berger, E. P.; Lansbury, P. T. Jr. The Carboxy Terminus of the .Beta. Amyloid Protein Is Critical for the Seeding of Amyloid Formation: Implications for the Pathogenesis of Alzheimer's Disease. *Biochemistry* **1993**, *32* (18), 4693–4697. https://doi.org/10.1021/bi00069a001.
- 1066 (38) Hoyer, W.; Cherny, D.; Subramaniam, V.; Jovin, T. M. Impact of the Acidic C-Terminal
  1067 Region Comprising Amino Acids 109–140 on α-Synuclein Aggregation in Vitro.
  1068 Biochemistry 2004, 43 (51), 16233–16242. https://doi.org/10.1021/bi048453u.
- 1069 (39) Campion, D.; Martin, C.; Heilig, R.; Charbonnier, F.; Moreau, V.; Flaman, J. M.; Petit, J. L.; 1070 Hannequin, D.; Brice, A.; Frebourg†, T. The NACP/Synuclein Gene: Chromosomal Assignment and Screening for Alterations in Alzheimer Disease. *Genomics* 1995, 26 (2), 254–257. https://doi.org/10.1016/0888-7543(95)80208-4.
- 1073 (40) Beyer, K.; Domingo-Sábat, M.; Lao, J. I.; Carrato, C.; Ferrer, I.; Ariza, A. Identification and Characterization of a New Alpha-Synuclein Isoform and Its Role in Lewy Body Diseases.

  Neurogenetics 2008, 9 (1), 15–23. https://doi.org/10.1007/s10048-007-0106-0.
- (41) Beyer, K.; Lao, J. I.; Carrato, C.; Mate, J. L.; López, D.; Ferrer, I.; Ariza, A. Differential
   Expression of α-Synuclein Isoforms in Dementia with Lewy Bodies. *Neuropathol. Appl.* Neurobiol. 2004, 30 (6), 601–607. https://doi.org/10.1111/j.1365-2990.2004.00572.x.
- 1079 (42) Beyer, K.; Humbert, J.; Ferrer, A.; Lao, J. I.; Carrato, C.; López, D.; Ferrer, I.; Ariza, A. Low
  1080 Alpha-Synuclein 126 mRNA Levels in Dementia with Lewy Bodies and Alzheimer Disease.
  1081 NeuroReport 2006, 17 (12), 1327–1330.
  1082 https://doi.org/10.1097/01.wnr.0000224773.66904.e7.
- 1083 (43) Beyer, K.; Domingo-Sabat, M.; Humbert, J.; Carrato, C.; Ferrer, I.; Ariza, A. Differential Expression of Alpha-Synuclein, Parkin, and Synphilin-1 Isoforms in Lewy Body Disease. *neurogenetics* **2008**, *9* (3), 163–172. https://doi.org/10.1007/s10048-008-0124-6.
- 1086 (44) McLean, J. R.; Hallett, P. J.; Cooper, O.; Stanley, M.; Isacson, O. Transcript Expression 1087 Levels of Full-Length Alpha-Synuclein and Its Three Alternatively Spliced Variants in 1088 Parkinson's Disease Brain Regions and in a Transgenic Mouse Model of Alpha-Synuclein

- 1089 Overexpression. *Mol. Cell. Neurosci.* **2012**, 49 (2), 230–239. https://doi.org/10.1016/j.mcn.2011.11.006.
- 1091 (45) Cardo, L. F.; Coto, E.; de Mena, L.; Ribacoba, R.; Mata, I. F.; Menéndez, M.; Moris, G.; Alvarez, V. Alpha-Synuclein Transcript Isoforms in Three Different Brain Regions from Parkinson's Disease and Healthy Subjects in Relation to the SNCA Rs356165/Rs11931074 Polymorphisms. *Neurosci. Lett.* **2014**, 562, 45–49. https://doi.org/10.1016/j.neulet.2014.01.009.
- 1096 (46) Brudek, T.; Winge, K.; Rasmussen, N. B.; Bahl, J. M. C.; Tanassi, J.; Agander, T. K.; Hyde, T. M.; Pakkenberg, B. Altered α-Synuclein, Parkin, and Synphilin Isoform Levels in Multiple 1097 1098 System Atrophy Brains. J. Neurochem. 2016. 136 (1),172–185. 1099 https://doi.org/10.1111/jnc.13392.
- (47) Röntgen, A.; Toprakcioglu, Z.; Tomkins, J. E.; Vendruscolo, M. Modulation of α-Synuclein
   in Vitro Aggregation Kinetics by Its Alternative Splice Isoforms. *Proc. Natl. Acad. Sci. USA* 2024, 121 (7), e2313465121. https://doi.org/10.1073/pnas.2313465121.
- (48) Röntgen, A.; Toprakcioglu, Z.; Dada, S. T.; Morris, O. M.; Knowles, T. P. J.; Vendruscolo,
   M. Aggregation of α-Synuclein Splice Isoforms through a Phase Separation Pathway. *Sci. Adv.* 2025, *11* (16), eadq5396. https://doi.org/10.1126/sciadv.adq5396.
- (49) SanGiovanni, D. Q.; McGlinchey, R. P.; Lee, J. C. Amyloid Formation of Alternatively
   Spliced Variants of α-Synuclein. Protein Sci. 2025, 34 (7), e70195.
   https://doi.org/10.1002/pro.70195.
- (50) McCarthy, J. J.; Linnertz, C.; Saucier, L.; Burke, J. R.; Hulette, C. M.; Welsh-Bohmer, K. A.;
  Chiba-Falek, O. The Effect of SNCA 3' Region on the Levels of SNCA-112 Splicing Variant.
  Neurogenetics 2011, 12 (1), 59–64. https://doi.org/10.1007/s10048-010-0263-4.
- 1112 (51) Fulcher, J. M.; Makaju, A.; Moore, R. J.; Zhou, M.; Bennett, D. A.; De Jager, P. L.; Qian, W.1113 J.; Paša-Tolić, L.; Petyuk, V. A. Enhancing Top-Down Proteomics of Brain Tissue with
  1114 FAIMS. J. Proteome Res. 2021, 20 (5), 2780–2795.
  1115 https://doi.org/10.1021/acs.jproteome.1c00049.
- (52) Bertoncini, C. W.; Jung, Y.-S.; Fernandez, C. O.; Hoyer, W.; Griesinger, C.; Jovin, T. M.;
   Zweckstetter, M. Release of Long-Range Tertiary Interactions Potentiates Aggregation of
   Natively Unstructured α-Synuclein. *Proc. Natl. Acad. Sci. USA* 2005, 102 (5), 1430–1435.
   https://doi.org/10.1073/pnas.0407146102.
- 1120 (53) Cho, M.-K.; Nodet, G.; Kim, H.-Y.; Jensen, M. R.; Bernado, P.; Fernandez, C. O.; Becker, S.; Blackledge, M.; Zweckstetter, M. Structural Characterization of α-Synuclein in an 1121 Aggregation 1122 Prone State. Protein Sci. 2009, 18 (9),1840-1846. https://doi.org/10.1002/pro.194. 1123
- (54) Dedmon, M. M.; Lindorff-Larsen, K.; Christodoulou, J.; Vendruscolo, M.; Dobson, C. M.
   Mapping Long-Range Interactions in α-Synuclein Using Spin-Label NMR and Ensemble
   Molecular Dynamics Simulations. J. Am. Chem. Soc. 2005, 127 (2), 476–477.
   https://doi.org/10.1021/ja044834j.
- 1128 (55) Wu, K.-P.; Kim, S.; Fela, D. A.; Baum, J. Characterization of Conformational and Dynamic Properties of Natively Unfolded Human and Mouse α-Synuclein Ensembles by NMR:

- 1130 Implication for Aggregation. *J. Mol. Biol.* **2008**, *378* (5), 1104–1115. https://doi.org/10.1016/j.jmb.2008.03.017.
- 1132 (56) Pedersen, M. E.; Østergaard, J.; Jensen, H. Flow-Induced Dispersion Analysis (FIDA) for 1133 Protein Quantification and Characterization. In *Clinical Applications of Capillary* 1134 *Electrophoresis: Methods and Protocols*; Phillips, T. M., Ed.; Springer: New York, NY, 2019; 1135 pp 109–123. https://doi.org/10.1007/978-1-4939-9213-3 8.
- 1136 (57) Tesei, G.; Lindorff-Larsen, K. Improved Predictions of Phase Behaviour of Intrinsically 1137 Disordered Proteins by Tuning the Interaction Range. *Open Res. Eur.* **2023**, *2*, 94. 1138 https://doi.org/10.12688/openreseurope.14967.2.
- 1139 (58) Tesei, G.; Trolle, A. I.; Jonsson, N.; Betz, J.; Knudsen, F. E.; Pesce, F.; Johansson, K. E.; Lindorff-Larsen, K. Conformational Ensembles of the Human Intrinsically Disordered Proteome. *Nature* **2024**, *626* (8000), 897–904. https://doi.org/10.1038/s41586-023-07004-5.
- (59) Meisl, G.; Kirkegaard, J. B.; Arosio, P.; Michaels, T. C. T.; Vendruscolo, M.; Dobson, C. M.; 1142 Linse, S.; Knowles, T. P. J. Molecular Mechanisms of Protein Aggregation from Global 1143 1144 Fitting of Kinetic Models. Nat. Protoc. 2016. 11 (2),252-272. 1145 https://doi.org/10.1038/nprot.2016.010.
- 1146 (60) Tseng, E.; Rowell, W. J.; Glenn, O.-C.; Hon, T.; Barrera, J.; Kujawa, S.; Chiba-Falek, O. The
  1147 Landscape of SNCA Transcripts Across Synucleinopathies: New Insights From Long Reads
  1148 Sequencing Analysis. *Front. Genet.* **2019**, *10*, 584.
  1149 https://doi.org/10.3389/fgene.2019.00584.
- (61) Buell, A. K.; Galvagnion, C.; Gaspar, R.; Sparr, E.; Vendruscolo, M.; Knowles, T. P. J.; Linse,
   S.; Dobson, C. M. Solution Conditions Determine the Relative Importance of Nucleation and
   Growth Processes in α-Synuclein Aggregation. *Proc. Natl. Acad. Sci. USA* 2014, *111* (21),
   7671–7676. https://doi.org/10.1073/pnas.1315346111.
- 1154 (62) Connor, J. P.; Radford, S. E.; Brockwell, D. J. Structural and Thermodynamic Classification of Amyloid Polymorphs. *Structure* **2025**, 0 (0). https://doi.org/10.1016/j.str.2025.07.005.
- 1156 (63) Sawaya, M. R.; Hughes, M. P.; Rodriguez, J. A.; Riek, R.; Eisenberg, D. S. The Expanding 1157 Amyloid Family: Structure, Stability, Function, and Pathogenesis. *Cell* **2021**, *184* (19), 4857– 1158 4873. https://doi.org/10.1016/j.cell.2021.08.013.
- 1159 (64) Michaels, T. C. T.; Dear, A. J.; Knowles, T. P. J. Universality of Filamentous Aggregation 1160 Phenomena. *Phys. Rev. E* **2019**, *99* (6), 062415. 1161 https://doi.org/10.1103/PhysRevE.99.062415.
- (65) Xu, C. K.; Meisl, G.; Andrzejewska, E. A.; Krainer, G.; Dear, A. J.; Castellana-Cruz, M.;
  Turi, S.; Edu, I. A.; Vivacqua, G.; Jacquat, R. P. B.; Arter, W. E.; Spillantini, M. G.;
  Vendruscolo, M.; Linse, S.; Knowles, T. P. J. α-Synuclein Oligomers Form by Secondary
  Nucleation. *Nat. Commun.* 2024, *15* (1), 7083. https://doi.org/10.1038/s41467-024-50692-4.
- 1166 (66) Wilkins, D. K.; Grimshaw, S. B.; Receveur, V.; Dobson, C. M.; Jones, J. A.; Smith, L. J. Hydrodynamic Radii of Native and Denatured Proteins Measured by Pulse Field Gradient NMR Techniques. *Biochemistry* **1999**, *38* (50), 16424–16431. https://doi.org/10.1021/bi991765q.

- 1170 (67) Yu, H.; Han, W.; Ma, W.; Schulten, K. Transient β-Hairpin Formation in α-Synuclein 1171 Monomer Revealed by Coarse-Grained Molecular Dynamics Simulation. *J. Chem. Phys.* 1172 **2015**, 143 (24), 243142. https://doi.org/10.1063/1.4936910.
- 1173 (68) Allison, J. R.; Rivers, R. C.; Christodoulou, J. C.; Vendruscolo, M.; Dobson, C. M. A Relationship between the Transient Structure in the Monomeric State and the Aggregation Propensities of α-Synuclein and β-Synuclein. *Biochemistry* **2014**, *53* (46), 7170–7183. https://doi.org/10.1021/bi5009326.
- 1177 (69) Pesce, F.; Newcombe, E. A.; Seiffert, P.; Tranchant, E. E.; Olsen, J. G.; Grace, C. R.; 1178 Kragelund, B. B.; Lindorff-Larsen, K. Assessment of Models for Calculating the Hydrodynamic Radius of Intrinsically Disordered Proteins. *Biophys. J.* **2023**, *122* (2), 310–1180 321. https://doi.org/10.1016/j.bpj.2022.12.013.
- 1181 (70) Kirkwood, J. G.; Riseman, J. The Intrinsic Viscosities and Diffusion Constants of Flexible
  1182 Macromolecules in Solution. *J. Chem. Phys.* **1948**, *16* (6), 565–573.
  1183 https://doi.org/10.1063/1.1746947.
- (71) Waszkiewicz, R.; Michaś, A.; Białobrzewski, M. K.; Klepka, B. P.; Cieplak-Rotowska, M. K.; Staszałek, Z.; Cichocki, B.; Lisicki, M.; Szymczak, P.; Niedzwiecka, A. Hydrodynamic Radii of Intrinsically Disordered Proteins: Fast Prediction by Minimum Dissipation Approximation and Experimental Validation. J. Phys. Chem. Lett. 2024, 15 (19), 5024–5033. https://doi.org/10.1021/acs.jpclett.4c00312.
- 1189 (72) Flory, P. J. The Configuration of Real Polymer Chains. *J. Chem. Phys.* **1949**, *17* (3), 303–1190 310. https://doi.org/10.1063/1.1747243.
- 1191 (73) Fernández, C. O.; Hoyer, W.; Zweckstetter, M.; Jares-Erijman, E. A.; Subramaniam, V.; Griesinger, C.; Jovin, T. M. NMR of A-synuclein–Polyamine Complexes Elucidates the Mechanism and Kinetics of Induced Aggregation. *EMBO J.* **2004**, *23* (10), 2039–2046. https://doi.org/10.1038/sj.emboj.7600211.
- 1195 (74) Simpson, E. H. The Interpretation of Interaction in Contingency Tables. *J. R. Stat. Soc. Ser.* 1196 *B Methodol.* **1951**, *13* (2), 238–241. https://doi.org/10.1111/j.2517-6161.1951.tb00088.x.
- (75) Kumari, P.; Ghosh, D.; Vanas, A.; Fleischmann, Y.; Wiegand, T.; Jeschke, G.; Riek, R.;
  Eichmann, C. Structural Insights into α-Synuclein Monomer–Fibril Interactions. *Proc. Natl. Acad. Sci. USA* 2021, *118* (10), e2012171118. https://doi.org/10.1073/pnas.2012171118.
- 1200 (76) Chen, D.; Drombosky, K. W.; Hou, Z.; Sari, L.; Kashmer, O. M.; Ryder, B. D.; Perez, V. A.; Woodard, D. R.; Lin, M. M.; Diamond, M. I.; Joachimiak, L. A. Tau Local Structure Shields an Amyloid-Forming Motif and Controls Aggregation Propensity. *Nat. Commun.* **2019**, *10*, 2493. https://doi.org/10.1038/s41467-019-10355-1.
- 1204 (77) Byrd, E. J.; Rowlinson, B.; Crossley, J. A.; Brockwell, D. J.; Ross, J. F.; Radford, S. E.; 1205 Sobott, F. Zn2+ Binding Shifts the Conformational Ensemble of α-Synuclein Monomers toward Amyloid Chem. 1206 Accelerated Formation. J. Am. Soc. 2025. 1207 https://doi.org/10.1021/jacs.5c11056.
- (78) Gaspar, R.; Lund, M.; Sparr, E.; Linse, S. Anomalous Salt Dependence Reveals an Interplay
   of Attractive and Repulsive Electrostatic Interactions in α-Synuclein Fibril Formation. *QRB Discov.* 2020, *I*, e2. https://doi.org/10.1017/qrd.2020.7.

- 1211 (79) Flynn, J. D.; McGlinchey, R. P.; Walker, R. L.; Lee, J. C. Structural Features of α-Synuclein 1212 Amyloid Fibrils Revealed by Raman Spectroscopy. *J. Biol. Chem.* **2018**, *293* (3), 767–776.
- 1213 https://doi.org/10.1074/jbc.M117.812388.
- 1214 (80) Ziaunys, M.; Sakalauskas, A.; Mikalauskaite, K.; Smirnovas, V. Polymorphism of Alpha-
- Synuclein Amyloid Fibrils Depends on Ionic Strength and Protein Concentration. *Int. J. Mol.*
- 1216 *Sci.* **2021**, *22* (22), 12382. https://doi.org/10.3390/ijms222212382.
- 1217 (81) Munishkina, L. A.; Henriques, J.; Uversky, V. N.; Fink, A. L. Role of Protein-Water
- Interactions and Electrostatics in α-Synuclein Fibril Formation. *Biochemistry* **2004**, *43* (11),
- 1219 3289–3300. https://doi.org/10.1021/bi034938r.
- 1220 (82) Horne, R. I.; Metrick, M. A.; Man, W.; Rinauro, D. J.; Brotzakis, Z. F.; Chia, S.; Meisl, G.;
- 1221 Vendruscolo, M. Secondary Processes Dominate the Quiescent, Spontaneous Aggregation of
- 1222 α-Synuclein at Physiological pH with Sodium Salts. ACS Chem. Neurosci. 2023, 14 (17),
- 1223 3125–3131. https://doi.org/10.1021/acschemneuro.3c00282.
- 1224 (83) Zacharopoulou, M.; Seetaloo, N.; Ross, J.; Stephens, A. D.; Fusco, G.; McCoy, T. M.; Dai,
- 1225 W.; Mela, I.; Fernandez-Villegas, A.; Martel, A.; Routh, A. F.; De Simone, A.; Phillips, J. J.;
- 1226 Kaminski Schierle, G. S. Local Ionic Conditions Modulate the Aggregation Propensity and
- Influence the Structural Polymorphism of α-Synuclein. J. Am. Chem. Soc. 2025, 147 (16),
- 1228 13131–13145. https://doi.org/10.1021/jacs.4c13473.
- 1229 (84) Byrd, E. J.; Wilkinson, M.; Radford, S. E.; Sobott, F. Taking Charge: Metal Ions Accelerate
- Amyloid Aggregation in Sequence Variants of α-Synuclein. J. Am. Soc. Mass Spectrom. 2023,
- 1231 34 (3), 493–504. https://doi.org/10.1021/jasms.2c00379.
- 1232 (85) Connor, J. P.; Radford, S. E.; Brockwell, D. J. Structural and Thermodynamic Classification
- of Amyloid Polymorphs. *Structure* **2025**, 0 (0). https://doi.org/10.1016/j.str.2025.07.005.
- 1234 (86) Wu, K.-P.; Weinstock, D. S.; Narayanan, C.; Levy, R. M.; Baum, J. Structural Reorganization
- of α-Synuclein at Low pH Observed by NMR and REMD Simulations. J. Mol. Biol. 2009,
- 1236 391 (4), 784–796. https://doi.org/10.1016/j.jmb.2009.06.063.
- 1237 (87) Kapasi, A.; Brosch, J. R.; Nudelman, K. N.; Agrawal, S.; Foroud, T. M.; Schneider, J. A. A
- Novel SNCA E83Q Mutation in a Case of Dementia with Lewy Bodies and Atypical
- 1239 Frontotemporal Lobar Degeneration. Neuropathol. Off. J. Jpn. Soc. Neuropathol. 2020, 40
- 1240 (6), 620–626. https://doi.org/10.1111/neup.12687.
- 1241 (88) Kumar, S. T.; Mahul-Mellier, A.-L.; Hegde, R. N.; Rivière, G.; Moons, R.; Ibáñez de Opakua,
- 1242 A.; Magalhães, P.; Rostami, I.; Donzelli, S.; Sobott, F.; Zweckstetter, M.; Lashuel, H. A. A
- NAC Domain Mutation (E83Q) Unlocks the Pathogenicity of Human Alpha-Synuclein and
- Recapitulates Its Pathological Diversity. Sci. Adv. 2022, 8 (17), eabn0044.
- 1245 https://doi.org/10.1126/sciadv.abn0044.
- 1246 (89) McGlinchey, R. P.; Ramos, S.; Dimitriadis, E. K.; Wilson, C. B.; Lee, J. C. Defining Essential
- 1247 Charged Residues in Fibril Formation of a Lysosomal Derived N-Terminal α-Synuclein
- Truncation. *Nat. Commun.* **2025**, *16*, 3825. https://doi.org/10.1038/s41467-025-58899-9.
- 1249 (90) Yang, X.; Wang, B.; Hoop, C. L.; Williams, J. K.; Baum, J. NMR Unveils an N-Terminal
- Interaction Interface on Acetylated-α-Synuclein Monomers for Recruitment to Fibrils. *Proc.*
- 1251 Natl. Acad. Sci. USA **2021**, 118 (18), e2017452118.
- 1252 https://doi.org/10.1073/pnas.2017452118.

- 1253 (91) Kjer-Hansen, P.; Phan, T. G.; Weatheritt, R. J. Protein Isoform-Centric Therapeutics: Expanding Targets and Increasing Specificity. *Nat. Rev. Drug Discov.* **2024**, 1–21. https://doi.org/10.1038/s41573-024-01025-z.
- 1256 (92) Adams, D.; Gonzalez-Duarte, A.; O'Riordan, W. D.; Yang, C.-C.; Ueda, M.; Kristen, A. V.; Tourney, I.; Schmidt, H. H.; Coelho, T.; Berk, J. L.; Lin, K.-P.; Vita, G.; Attarian, S.; Planté-1257 1258 Bordeneuve, V.; Mezei, M. M.; Campistol, J. M.; Buades, J.; Brannagan, T. H.; Kim, B. J.; 1259 Oh, J.; Parman, Y.; Sekijima, Y.; Hawkins, P. N.; Solomon, S. D.; Polydefkis, M.; Dyck, P. J.; Gandhi, P. J.; Goyal, S.; Chen, J.; Strahs, A. L.; Nochur, S. V.; Sweetser, M. T.; Garg, P. 1260 1261 P.; Vaishnaw, A. K.; Gollob, J. A.; Suhr, O. B. Patisiran, an RNAi Therapeutic, for Hereditary 1262 Transthyretin Amyloidosis. Ν. Engl. J. Med. 2018. 379 (1),11–21. https://doi.org/10.1056/NEJMoa1716153. 1263
- 1264 (93) Pedregosa, F.; Varoquaux, G.; Gramfort, A.; Michel, V.; Thirion, B.; Grisel, O.; Blondel, M.;
  1265 Prettenhofer, P.; Weiss, R.; Dubourg, V.; Vanderplas, J.; Passos, A.; Cournapeau, D.; Brucher,
  1266 M.; Perrot, M.; Duchesnay, É. Scikit-Learn: Machine Learning in Python. *J. Mach. Learn.*1267 *Res.* **2011**, *12* (85), 2825–2830.
- 1268 (94) Cohen, S. I. A.; Vendruscolo, M.; Welland, M. E.; Dobson, C. M.; Terentjev, E. M.; Knowles, T. P. J. Nucleated Polymerization with Secondary Pathways I. Time Evolution of the Principal Moments. *J. Chem. Phys.* **2011**, *135* (6), 065105. https://doi.org/10.1063/1.3608916.

1271

1272

1273

1274

1275

1276

1277

1278

1279

1280

# 1281 For Table of Contents Only

